

Comparison of the quasi-steady-state heat transport in phase-change and classical Rayleigh-Bénard convection for a wide range of Stefan number and Rayleigh number

Cite as: Phys. Fluids **31**, 096605 (2019); <https://doi.org/10.1063/1.5110295>

Submitted: 17 May 2019 . Accepted: 09 August 2019 . Published Online: 24 September 2019

Ojas Satbhai , Subhransu Roy, Sudipto Ghosh, Suman Chakraborty , and Rajaram Lakkaraju 



View Online



Export Citation



CrossMark

ARTICLES YOU MAY BE INTERESTED IN

[Maximum spreading of droplets impacting spherical surfaces](#)

Phys. Fluids **31**, 092102 (2019); <https://doi.org/10.1063/1.5117278>

[Spectral energy transfer in a viscoelastic homogeneous isotropic turbulence](#)

Phys. Fluids **31**, 095105 (2019); <https://doi.org/10.1063/1.5112161>

[Front dynamics in exchange flow of two immiscible iso-viscous fluids in two-dimensional straight and curved plane channels](#)

Phys. Fluids **31**, 092105 (2019); <https://doi.org/10.1063/1.5108748>

SciLight

Highlights of the best new research
in the physical sciences

AIP
Publishing

LEARN MORE

Comparison of the quasi-steady-state heat transport in phase-change and classical Rayleigh-Bénard convection for a wide range of Stefan number and Rayleigh number

Cite as: Phys. Fluids 31, 096605 (2019); doi: 10.1063/1.5110295

Submitted: 17 May 2019 • Accepted: 9 August 2019 •

Published Online: 24 September 2019



View Online



Export Citation



CrossMark

Ojas Satbhai,^{1,2,a} Subhransu Roy,¹ Sudipto Ghosh,³ Suman Chakraborty,¹ and Rajaram Lakkaraju¹

AFFILIATIONS

¹ Department of Mechanical Engineering, Indian Institute of Technology Kharagpur, Kharagpur 721302, West Bengal, India

² Department of Mechanical Engineering, School of Technology, Pandit Deendayal Petroleum University, Gandhinagar 382007, Gujarat, India

³ Department of Metallurgical & Materials Engineering, Indian Institute of Technology Kharagpur, Kharagpur 721302, West Bengal, India

^aAuthor to whom correspondence should be addressed: satbhaiojas@gmail.com and ojas.satbhai@sot.pdpu.ac.in

ABSTRACT

We report the first comparative study of the phase-change Rayleigh–Bénard (RB) convection system and the classical RB convection system to systematically characterize the effect of the oscillating solid–liquid interface on the RB convection. Here, the role of Stefan number Ste (defined as the ratio between the sensible heat to the latent heat) and the Rayleigh number based on the averaged liquid height \bar{Ra}_f is systematically explored with direct numerical simulations for low Prandtl number fluid ($\text{Pr} = 0.0216$) in a phase-change RB convection system during the stationary state. The control parameters \bar{Ra}_f ($3.96 \times 10^4 \leq \bar{Ra}_f \leq 9.26 \times 10^7$) and Ste ($1.1 \times 10^{-2} \leq \text{Ste} \leq 1.1 \times 10^2$) are varied over a wide range to understand its influence on the heat transport and flow features. Here, we report the comparison of large-scale motions and temperature fields, frequency power spectra for vertical velocity, and a scaling law for the time-averaged Nusselt number at the hot plate \bar{Nu}_h vs \bar{Ra}_f for both the RB systems. The intensity of solid–liquid interface oscillations and the standard deviation of Nu_h increase with the increase in Ste and \bar{Ra}_f . There are two distinct RB flow configurations at low \bar{Ra}_f independent of Ste . At low and moderate \bar{Ra}_f , the ratio of the Nusselt number for phase-change RB convection to the Nusselt number for classical RB convection $\bar{Nu}_h/\bar{Nu}_h^{RB}$ is always greater than one. However, at higher \bar{Ra}_f , the RB convection is turbulent, and $\bar{Nu}_h/\bar{Nu}_h^{RB}$ can be less than or greater than one depending on the value of Ste . The results may turn out to be of immense consequence for understanding and altering the transport characteristics in the phase-change RB convection systems.

Published under license by AIP Publishing. <https://doi.org/10.1063/1.5110295>

I. INTRODUCTION

In a solid–liquid phase-change process, the Stefan number, Ste , defined as the ratio of the sensible heat to the latent heat, plays an important role in the dynamics of heat transport. The Stefan number may dictate natural convection phenomenon rather nontrivially, establishing a rich interplay between fluid dynamics and thermal transport over the relevant spatio-temporal scales.^{4,5,11} Such confluences may have far-ranging implications in the fields of engineering^{1,4,5,35} and natural sciences.^{7,12,18,20,37,43} However, the role of the Stefan number in Rayleigh–Bénard (RB) convection

accompanying phase-change has not been explicitly brought out in the reported literature. For example, the roll-type flow structures formed in classical RB convection⁴¹ are likely to get somewhat distorted due to the release or absorption of latent heat; this, in turn, may alter the resulting transport in a nontrivial manner. In various melting and/or solidification systems in engineering and technological application viz., storage of thermal energy,^{30,44} liquid melt pool formed in the reactor lower head in the late phase of nuclear accident,¹ phase changed material (PCM) based transient cooling systems for mobile, and stationary electronic devices^{5,35} phase change material can either be natural or synthetic. Material scientists and

thermal equipment designers do not have any guidelines on the relationship between Stefan and global heat transport.

Liquid melts of pure metals and eutectic alloys cooled on one side and heated on the other side offer unstable density gradients and drive the convection currents. In the case of alloys, the solute gradient in the liquid melt in addition to the temperature gradient leads to the unstable density gradients. Mushy region formation between the solid and liquid phase has been extensively studied for the plume, chimney, and freckle formation.^{17,42} Earlier works have considered both fluid flow and heat transfer features with some inclusions of kinetics.^{4,5} However, studies on any influence of the Stefan number over the flow and plume structures, large-scale motions, melt volume fraction evolution, melt-front dynamics, and global heat transport in the presence of strong temperature gradients are missing.

Natural convection with melting and/or solidification^{4–6,8,16,37} has been a popular subject of research. However, to the best of the authors' knowledge, the above-mentioned vital questions regarding the role of the Stefan number on the RB convection remain unanswered. The role of the geometrical shape and the aspect ratio of the enclosures on the RB convection have been studied in the past,^{2,10,24,45} however, the role of the aspect ratio of the effective flow region and on the RB convection due to the nonplanar melting/solidifying boundaries during the stationary state is not yet studied. Here, we attempt to bring out some general features pertaining to the role of the Stefan number in RB convection accompanying melting and solidification transport. The dynamics of the phase-change substance in RB-like convection is complex and additionally depends on the Stefan number, Ste . Usually, for pure materials and eutectic alloys, the molten liquid and solid zones are macroscopically separated by a sharp solid-liquid interface, and the solid-liquid interface shows spatio-temporal oscillations (see Fig. 1). Through the sharp interface, the thermal energy conducts into the solid part and finally leaves through the cold plate. The heat transport and flow dynamics for a phase-change substance undergoing melting and solidification in RB convection involving oscillating solid-liquid interface are still unexplored in the scientific community, especially, over a wide range of Ste and at relatively higher Rayleigh numbers.

In this work, we try to find out how the stationary state phase-change Rayleigh–Bénard convection with an oscillating solid-liquid interface differs from a classical Rayleigh–Bénard convection in terms of time-averaged temperature, convective flow field, and heat transport over a range of Rayleigh numbers encompassing laminar unsteady to turbulent regimes. The numerical study is performed by solving the complete Navier–Stokes equation and energy equation using direct numerical simulations. We study the influence of the Stefan number on the spatio-temporal oscillations of the solid-liquid interface during the stationary state over a range of Rayleigh numbers. The real-time flows, especially turbulent flows, are three-dimensional in nature, and the three-dimensional DNS simulations are necessary to accurately estimate the steady-state Nusselt numbers. From earlier rigorous computational studies,^{23,33} it is expected that at low Prandtl numbers, the two-dimensional DNS solutions will overestimate the average Nusselt number and underpredict its fluctuations because in two-dimensional simulations, the poloidal motions are captured, but the toroidal motions are not captured. However, the insightful outcome of the influence of Ste and Ra on

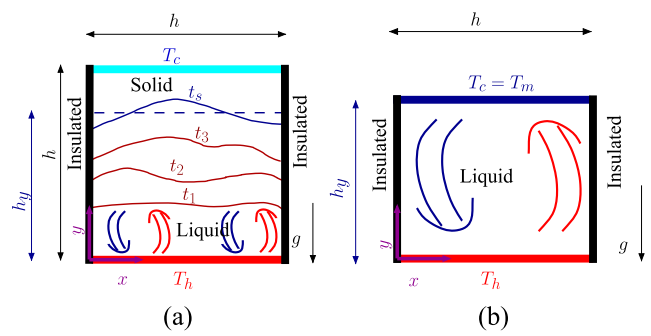


FIG. 1. Schematic diagram for two different RB systems (a) two-phase RB convection system and (b) single phase RB convection system. In both the RB systems, the bottom boundary (relatively hot) and the top boundary (relatively cold) which encompass the liquid zone have a fixed temperature T_h and T_m , while the sidewalls are insulated. Figure 1(a) shows the schematic of a phase-change Rayleigh–Bénard (RB) convection during the melting process in a two-dimensional unit aspect ratio box (i.e., length = width = h). The bottom and top boundaries have a fixed temperature T_h and T_c (such that $T_c < T_m < T_h$), while the side-walls are insulated. Both brown and blue colored continuous lines show the melt-front (isocontour of T_m) position at different times. The melt-front positions during the transient regime ($t < t_s$) for the phase-change RB system are shown by the brown lines, whereas the time-averaged position of the melt-front during the oscillatory solidification-melting regime ($t \geq t_s$) is shown by the blue continuous lines. The dotted blue line shows the space average position $h_y = \frac{1}{h} \int_0^h h_i(x) dx$ of the time-averaged melt-front during the oscillatory solidification-melting regime, where $h_i(x)$ is the ordinate of time-averaged melt-front for each x coordinate.

the heat transport obtained from the comparatively less CPU (Central Processing Unit) intensive 2D DNS study is still valid, and the overestimation of the Nusselt number from the 2D studies in comparison with 3D studies is well documented (see Refs. 23 and 33 and Sec. A 3 in Appendix A).

II. MATHEMATICAL AND COMPUTATIONAL MODEL

A. Physical system and governing equations

In this work, we intend to study the influence of the phase-change (melting/solidifying) boundary which apart from being an isothermal cold boundary at T_m in the Rayleigh–Bénard system can also absorb/release the latent heat from/to the adjacent liquid/solid phase. The two-dimensional square box (of equal length and height h) isothermally heated at the bottom wall (at T_h), isothermally cooled at the top wall (at T_c), and insulated on the sides as shown in Fig. 1(a). Figure 1(b) represents a classical RB system which acts as the reference system to analyze the phase-change Rayleigh–Bénard (RB) system. In both the systems initially, the working fluid inside the box is maintained at the initial temperature T_i . In the case of the phase-change RB system, the initial temperature T_i is less than the melt temperature T_m , i.e., initially the phase change material (PCM) material is solid. The thermal energy entering from the bottom plate is partitioned between latent heat (melting the solid) and sensible heat (warming the fluid). Here, the PCM material is a pure material, and the molten liquid and solid zones are macroscopically separated by a sharp melt-front [see Fig. 1(a)]. Until the onset of convection, the melting is expected to happen by the diffusion process; thus, the melt-front is expected to be flat initially.⁸ After the onset of

convection, the upward moving melt-front shows spatio-temporal oscillations due to the onset of fluid flow. The melt-front finally ($t \geq t_s$) equilibrates to a quasisteady position, where it oscillates about the time-averaged position; t_s is the instant of time for initiation of the quasisteady oscillatory solidification-melting regime. The time-averaged position is shown by a continuous blue line in Fig. 1(a), and the flat dashed blue line shows the horizontally-averaged position $h_y = \frac{1}{h} \int_0^h h_l(x) dx$ of the time-averaged melt-front during the oscillatory solidification-melting regime. Thus, for the phase-change Rayleigh-Bénard (RB) system, the time-averaged and horizontally averaged aspect ratio (AR) of the liquid zone is h_y/h . Figure 1(b) shows the schematic diagram of an equivalent pure Rayleigh-Bénard (RB) convection system which comprises of fluid inside the rectangular box with aspect ratio AR = h_y/h , heated isothermally from the bottom at temperature T_h and cooled isothermally from the top wall at temperature T_m . Note that the fluid for the pure RB system is identical as the fluid in the phase-change Rayleigh-Bénard (RB) system with only one difference that the fluid for the pure RB system does not solidify. As compared to single-phase/classical RB convection, the phase-change Rayleigh-Bénard convection has the solid-liquid interface as the cold isothermal boundary at the melt temperature T_m and this boundary also has the additional transport of latent heat based on the Stefan boundary condition.²¹ In this work, we are only going to study and compare the characteristics of both the phase-change and classical RB systems during the statistically stationary state, i.e., the time-averaged and dynamic heat transfer and flow characteristics of both the RB systems during the stationary state.

Usually, the rising and falling convective motions take place due to local temperature differences, and a deviation from mean temperature, $T_{avg} = (T_h + T_m)/2$, determines the system's dynamics. If a sufficient temperature difference, $\Delta' = T_h - T_{avg}$, is available such that the Rayleigh number is supercritical (see Refs. 4 and 38), then the liquid in the box shows convective rolls and rising and falling plumes instead of quiescent conduction layers. In this case, the convective heat transport is larger than conductive heat transport. In the Rayleigh-Bénard (RB) convection, the system dynamics are governed by the Rayleigh number based on fluid zone height $Ra_f = \rho g_0 \beta (T_h - T_m) h_y^3 / (\mu \alpha_{th})$ and the Prandtl number $Pr = \mu c/k$, where ρ is the density, g_0 is the acceleration due to gravity, β is the volumetric expansion coefficient, μ is the dynamic viscosity, k is the thermal conductivity, c is the specific heat, and $\alpha_{th} = k/\rho c$ is the thermal diffusivity. However, for the phase-change RB system, the fluid zone height is explicitly not known beforehand. Therefore, a system scale Rayleigh number Ra is defined based on the length scale h and $\Delta = 2\Delta' = T_h - T_c$. However, after performing the numerical experiments, average fluid zone height h_y becomes known, and Rayleigh number based on fluid zone height Ra_f can be calculated for phase-change RB system. In this work, for every phase-change RB system, there is an equivalent classical RB system which has the same value of Ra_f and the same aspect ratio of the fluid domain as that of the phase-change RB system. The Stefan number is defined as the ratio of the sensible heat to the latent heat $Ste = \rho c(T_h - T_m)/(\rho L) = \rho c(T_h - T_c)/(2 \times \rho L)$, where L is the latent heat of phase-change. The scales used in this work are h for length, $U_0 = \alpha_{th}/h$ for velocity (based on thermal diffusion), and $t_o = h/U_0$ for time. The dimensionless time used to report our simulations is $\tau = t/(h/U_0)$, where t is the dimensional time. Based on the above

dimensionless parameters, the dimensionless heat transport, the dimensionless velocity, and temperature fields are evaluated. The heat transport in the system is usually expressed as a dimensionless parameter popularly known as the Nusselt number. Here, the Nusselt number at the hot plate Nu_h and at the cold plate Nu_c are the Nusselt number averaged over the length of plate l_p . Here, the Nusselt number is defined as the ratio of the total heat flux, Q^T , entered from the plate (hot or cold) in the direction normal to the plate \hat{n} to the reference heat flux only due to conduction mode of heat transfer, Q^c . Mathematically, $Nu = \frac{1}{l_p} \int_0^{l_p} (Q^T/Q^c) dl$, where $Q^T = \int_0^{l_p} k \nabla T \cdot \hat{n} dl$ and $Q^c = \int_0^{l_p} k \frac{(T_h - T_m)}{h} dl$. Note that here \hat{n} is the direction normal to the hot or cold plate. At the stationary state, the time-averaged heat flux entered through the bottom plate equals the heat flux leaving from the melt-front and top plate. The heat transport and rising/falling motions increase with Raf .¹⁴ In our work, we have explored phase-change RB convection in detail through direct numerical simulations for the range $3.96 \times 10^4 \leq Raf \leq 9.26 \times 10^7$ and $1.14 \times 10^{-2} < Ste < 1.14 \times 10^2$.

In order to model solidification and melting with thermal convection, we assume that the phase-change (melting/solidification) is happening at local thermal equilibrium with the isothermal condition, the fluid is Newtonian and incompressible, and the Boussinesq approximation is valid. The thermophysical properties of both the liquid and solid phases are identical and assumed to be constant within the small temperature range across the system. See the work of Satbhai, Roy, and Ghosh^{27,29,30} for the validity of the assumptions and systems for which these are applicable.

The popular enthalpy-porosity method on fixed grids is used in our simulations to understand RB-like convection accompanied by melting and solidification.^{3,34,39,40} The dimensionless governing equations for the mass, momentum, and energy conservation for a phase-change problem are given by Brent, Voller, and Reid,³ Voller, Brent, and Prakash,³⁹ as

$$\nabla \cdot \mathbf{V} = 0, \quad (1)$$

$$\frac{D\mathbf{V}}{D\tau} = -\nabla p + Pr\nabla^2\mathbf{V} + PrRa\theta - PrA\mathbf{V}, \quad (2)$$

$$\frac{D\theta}{D\tau} = \nabla^2\theta - \frac{1}{Ste} \frac{\partial F}{\partial \tau}, \quad (3)$$

where \mathbf{V} is the dimensionless velocity vector normalized by the diffusion velocity U_o , i.e., $\mathbf{V} = (U_x\hat{i} + U_y\hat{j})/U_o$, p is the dimensionless pressure normalized by ρU_o^2 . The source term in the momentum equation [see Eq. (2)] is different for solid, liquid, and mushy zone. Here, A is the porosity-function specified in Eq. (4); the form of the porosity-function is derived from the Carman-Kozeny equation^{39,40}

$$A = \frac{C_1 h}{\rho U_o} \left[\frac{(1-F)^2}{(F^3 + b)} \right]. \quad (4)$$

In Eq. (4), C_1 is the morphological constant and accounts for the permeability constant based on the morphology inside the mushy zone, b is a numerical constant to avoid division by zero, and F is the liquid volume fraction at a given location which has a value of unity in the liquid phase, zero in the solid phase, and all values in-between zero and unity denote a mushy zone. The fluid fraction F is a Heaviside

function for isothermal melting; its value is determined iteratively using the source update method.^{21,25,34} Note that the Heaviside function for isothermal melting restricts the mushy zone to a very small value (see Refs. 30 and 36 for further details). Equation (2) is valid for the solid phase, liquid phase, and mushy phase. The dimensionless normalized morphological constant $\frac{C_1 h}{\rho U_o}$ has a large value (298.04×10^3) and b has to be a small value (10^{-4}).^{21,25,34} In the liquid phase ($F = 1$), Eq. (4) ensures that the value of the source terms is zero, and the classical Boussinesq equations are retrieved. In the solid zone ($F = 0$), the numerical model ensures that the source term dominates over all other terms in the momentum equations, thus effectively creating a zero velocity field in the solid phase. The mushy zone ($0 < F < 1$) is a mixture of the solid and liquid phases and modeled by a porouslike medium. In the mushy zone, the source term dominates over the transient, diffusive, and convective terms, and thus, the momentum equation approximates the Darcy law.⁴⁰ The source term in the energy equation ($-\frac{1}{Ste} \frac{\partial F}{\partial T}$) accounts for the absorption or release of phase-change heat; see the work of Satbhai, Roy, and Ghosh,^{27,29} Voller, Brent, and Prakash,³⁹ and Voller and Prakash⁴⁰ for other details. The global melt fraction F_L is defined as

the ratio of the liquid volume to the box volume. Note that at the stationary state, $\overline{F_L} = \frac{h_y}{h}$ and $Ra_f = 0.5 \times Ra \times F_L^3$. In our simulations, initially, the entire cavity is filled with the subcooled solid phase at a temperature slightly below the melting temperature ($\theta < \theta_m$), such that the dimensionless temperature $\theta = (T - T_m)/(T_h - T_m) = -0.06$. The bottom hot boundary at $y/h = 0$ is at $\theta = \theta_h = 1$, the top cold boundary (for $y/h = 1$) is at $\theta = \theta_c = -1$, and the left and right wall are perfectly insulated, i.e., at $x/h = 0$ and $x/h = 1$, $\nabla \theta = 0$. All the four walls of the box have no-slip ($U_x/U_o = 0$) and no penetration ($U_y/U_o = 0$) velocity boundary conditions. The mean temperature of the system corresponds to melting temperature $\theta_{avg} = \theta_m = \frac{\theta_h + \theta_c}{2} = 0$.

B. Numerical approach

The mentioned transport equations [Eqs. (1)–(3)] are discretized using the finite volume method on two-dimensional unstructured formulation using the OpenFOAM® platform; see the work of Jasak,¹³ Moukalled *et al.*,²² Satbhai,²⁶ Satbhai, Roy, and Ghosh^{27,29,31} for details. The spatial terms are discretized with second-order accurate schemes. The convective terms are

TABLE I. The parameters for each simulation case such as case number, grid resolution, system scale Rayleigh number Ra based on the length scale h and $\Delta = 2\Delta' = T_h - T_c$, Rayleigh number Ra_f based on the fluid height and temperature difference across the fluid layer $\Delta' = T_h - T_m$; Stefan number Ste, the flow configurations (P and Q) observed at low Rayleigh numbers, stationary state time-averaged Nusselt number at the hot plate \overline{Nu}_h , the standard deviation σ from the mean value of \overline{Nu}_h are summarized from column 1 to column 9, respectively. Note that A.0, B.0, C.0, and D.0 are for equivalent classical Rayleigh-Bénard convection, and they have the same Ra_f as that of respective cases for the phase-change RB system.

	$N_x \times N_Y$	Ra	Ra_f	Ste	Configuration	AR (h_y/h)	\overline{Nu}_h	σ
A.0	128×92	...	3.96×10^4	0.72	3.42	0.052
A.1	128×128	2.1×10^5	3.96×10^4	1.14×10^2	P	0.72	3.76	0.059
A.2	128×128	2.1×10^5	3.96×10^4	1.14×10^1	P	0.72	3.75	0.066
A.3	128×128	2.1×10^5	3.96×10^4	1.14×10^0	P	0.72	3.74	0.068
A'.3	128×128	2.1×10^5	3.96×10^4	1.14×10^0	Q	0.72	3.90	0.213
A.4	128×128	2.1×10^5	3.96×10^4	1.14×10^{-1}	P	0.72	3.76	0.070
A'.4	128×128	2.1×10^5	3.96×10^4	1.14×10^{-1}	Q	0.72	3.90	0.222
A.5	128×128	2.1×10^5	3.96×10^4	1.14×10^{-2}	P	0.72	3.76	0.070
A'.5	128×128	2.1×10^5	3.96×10^4	1.14×10^{-2}	Q	0.72	3.90	0.218
B.0	192×161	...	6.40×10^5	0.84	6.51	1.248
B.1	192×192	2.1×10^6	6.40×10^5	1.14×10^2	...	0.84	7.18	1.376
B.2	192×192	2.1×10^6	6.40×10^5	1.14×10^1	...	0.84	7.24	1.368
B.3	192×192	2.1×10^6	6.40×10^5	1.14×10^0	...	0.84	7.33	1.415
B.4	192×192	2.1×10^6	6.40×10^5	1.14×10^{-1}	...	0.84	7.31	1.420
B.5	192×192	2.1×10^6	6.40×10^5	1.14×10^{-2}	...	0.84	7.29	1.418
C.0	250×227	...	8.08×10^6	0.91	11.87	1.20
C.1	250×250	2.1×10^7	8.08×10^6	1.14×10^2	...	0.91	11.54	1.873
C.2	250×250	2.1×10^7	8.08×10^6	1.14×10^1	...	0.91	11.73	1.902
C.3	250×250	2.1×10^7	8.08×10^6	1.14×10^0	...	0.91	11.69	1.939
C.4	250×250	2.1×10^7	8.08×10^6	1.14×10^{-1}	...	0.91	12.53	2.177
C.5	250×250	2.1×10^7	8.08×10^6	1.14×10^{-2}	...	0.91	12.80	2.267
D.0	450×426	...	9.26×10^7	0.95	20.93	3.26
D.1	450×450	2.1×10^8	9.26×10^7	1.14×10^2	...	0.95	20.06	3.377
D.2	450×450	2.1×10^8	9.26×10^7	1.14×10^{-1}	...	0.95	21.20	3.385

discretized using a blend of 75% central difference scheme and 25% second-order linear upwind scheme.^{9,13,26} The transient terms are discretized using the first-order Euler implicit difference scheme with a dynamic time step.²² Throughout our simulations, the Courant number^{9,13,22} is restricted to 0.25 and is used to calculate the next computational time step. The Pressure Implicit Split Operator (PISO) algorithm is used for pressure-velocity calculations, and the velocities at the face centers of the mesh are obtained from the Rhee-Chow interpolation.⁹ The resulting linear system of equations is solved by using the preconditioned biconjugate gradient solver.^{9,13,22} During the numerical simulation, the time increment is carried out only if the solutions at each time step are converged with a mass residual less than 10^{-7} , and individual residuals for the temperature and velocity are less than 10^{-6} , otherwise inner cycles of the algorithm are repeated for the same time-step until convergence takes place.

In Table I, simulation parameters and resolution details are mentioned. Throughout the simulation, it is ensured that both the velocity and temperature boundary layers are captured well by providing higher resolution grid near the boundaries. First of all, the computational method was rigorously validated with multiple test cases for natural convection—driven melting/solidification and Rayleigh-Bénard convection benchmark problems. Details of the comparison of current numerical results with experimental and numerical benchmark cases are provided in some of our earlier works^{28–31} and Appendix A (see the supplementary material).

After validating our code for the mentioned test case, we have proceeded to simulate phase-change RB convection. In Table I, four sets of simulations for four different Rayleigh numbers based on average liquid height $Ra_f = 3.96 \times 10^4$ (Set A), $Ra_f = 6.40 \times 10^5$ (Set B), $Ra_f = 8.08 \times 10^6$ (Set C), and $Ra_f = 9.26 \times 10^7$ (Set D) are shown. In each set, a classical RB convection and several cases with phase-change RB convection for different Stefan number (Ste) are presented. In total, 24 simulations are presented excluding simulations for grid independence checks, simulations for flow configuration repeatability checks (described in Sec. III), and simulations for validation of the code. Briefly, the table consists of grid size in x and y directions, Ra_f , Ste, the kind of flow configuration (P and Q) described later in Sec. III, stationary state time-averaged Nusselt number at the hot plate \overline{Nu}_h , the measure of wall heat flux fluctuations or standard deviation σ from the mean value of \overline{Nu}_h . In our simulations, all the reported time-averaged fields (temperature, velocity field, etc.) and time-averaged bulk (area or volume-averaged) scalar parameters like \overline{Nu}_h averages are computed for long times ~ 575 eddy-turnover time units. Here, the eddy-turnover t_e is defined as the time required for a fluid chunk to travel twice the distance of the melt layer at the stationary state with the volume-averaged root mean square of vertical velocity $\langle U_y^{rms} \rangle$, mathematically, $t_e = \frac{2 \times h_y}{\langle U_y^{rms} \rangle}$.

III. RESULTS AND DISCUSSION

A. Melt dynamics in the stationary state

In the phase-change RB convection system, there is a cold solid layer on the top of a hot liquid melt; liquid melt has large-scale motions due to the Rayleigh-Bénard convection. Figures 2(a) and 2(b) show the solid-liquid interface positions for multiple instants in

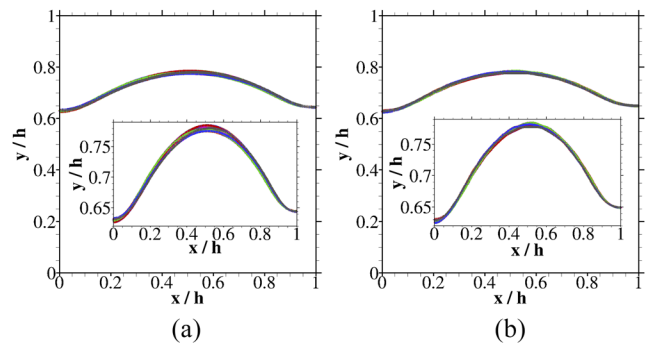


FIG. 2. 300 different positions of the solid-liquid interface at $Ra_f = 3.96 \times 10^4$ during the stationary state at a interval of $1/t_0$ for two different Stefan numbers: (a) $Ste = 1.14 \times 10^2$ and (b) $Ste = 1.14 \times 10^{-1}$. Note that different colors depict different positions of the solid-liquid interface at different times.

the stationary state for $Ra_f = 3.96 \times 10^4$ at the high Stefan number ($Ste = 1.14 \times 10^2$) and the low Stefan number ($Ste = 1.14 \times 10^{-1}$), respectively. Similarly, Figs. 3(a) and 3(b) show the solid-liquid interface positions for multiple instants of time in the stationary state for $Ra_f = 8.08 \times 10^6$ at the high Stefan number ($Ste = 1.14 \times 10^2$) and the low Stefan number ($Ste = 1.14 \times 10^{-1}$), respectively. As the heat transfer increases with the increase in the Rayleigh number, the top-solid-layer becomes thinner to allow a higher rate of heat conduction. It can be seen from the inset of Figs. 2(a), 2(b), 3(a), and 3(b) that the deviation of the solid-liquid interface from its time-averaged position is higher for the large Stefan number ($Ste = 1.14 \times 10^2$) as compared to the small Stefan number ($Ste = 1.14 \times 10^{-1}$) and this difference is more pronounced at high Ra_f ($Ra_f = 8.08 \times 10^6$). The inset of Figs. 3(a) and 3(b) show many undulations on the solid-liquid interface at any given time instant, and the amplitude of these undulations decreases as the Stefan number decreases from $Ste = 1.14 \times 10^2$ to $Ste = 1.14 \times 10^{-1}$. These undulations are the consequences of the melting (or solidification) event occurring when the liquid beneath the solid-liquid interface is able to supply (or absorb) the latent heat required for the phase-change. Therefore,

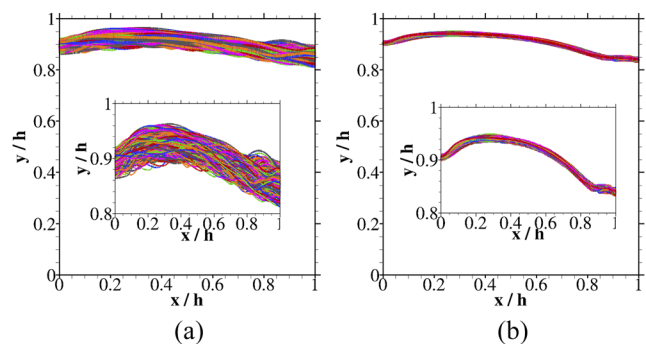


FIG. 3. 300 different positions of the solid-liquid interface at $Ra_f = 8.08 \times 10^6$ during the stationary state at a interval of $0.25/t_0$ for two different Stefan numbers: (a) $Ste = 1.14 \times 10^2$ and (b) $Ste = 1.14 \times 10^{-1}$. Note that different colors depict different positions of the solid-liquid interface at different times.

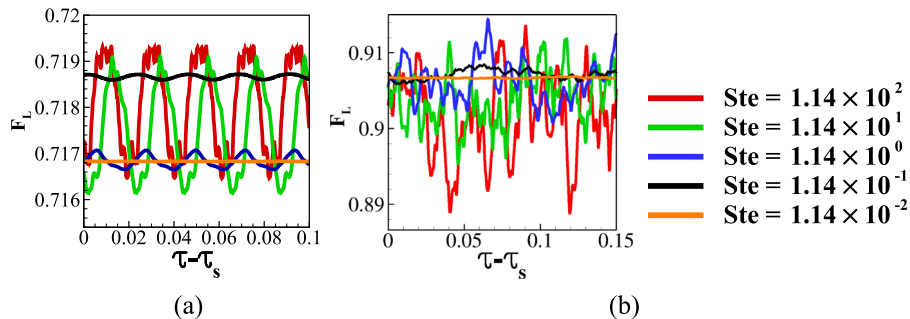


FIG. 4. Global liquid volume fraction F_L vs the nondimensional time $\tau - \tau_s$ for five different values of Ste during the stationary state at different Rayleigh numbers: (a) $Ra_f = 3.96 \times 10^4$ and (b) $Ra_f = 8.08 \times 10^6$. The nondimensional time corresponding to the arrival of the stationary state, τ_s is different for every case; thus, here F_L is plotted with respect to the modified nondimensional time $\tau - \tau_s$. Note that in Fig. 4(a), the curves for $Ste = 1.14 \times 10^{-2}$ and $Ste = 1.14 \times 10^0$ are with flow configuration-Q, while remaining three curves at $Ste = 1.14 \times 10^2$, 1.14×10^1 , and 1.14×10^{-1} are with flow configuration-P.

such undulations reduce with the decrease in Ste. The effects of the undulations of the solid-liquid interface on the flow field and temperature field of phase-change Rayleigh-Bénard convection will be elaborately discussed later in Sec. III B 3.

Figures 4(a) and 4(b) show the fluid fraction F_L vs the nondimensional time $\tau - \tau_s$ for $Ra_f = 3.96 \times 10^4$ and $Ra_f = 8.08 \times 10^6$ during the stationary state, i.e., for $\tau > \tau_s$. It can be seen that the time-averaged value of the global melt fraction \bar{F}_L increases or the thickness of the top-solid-layer decreases as Ra_f increases from 3.96×10^4 to 8.08×10^6 . The fluctuations of F_L seen in Figs. 4(a) and 4(b) represent the fluctuating liquid-phase volume or oscillating solid-liquid interface as a consequence of melting dynamics at the stationary state. From the melting dynamics at the stationary state, it is seen that at low Ra_f , the flow is almost periodic and unsteady and becomes turbulent at high Ra_f ; detailed quantification is described later in Sec. III B 1. It is seen that the amplitude of the solid-liquid interface oscillations increases with the increase in the Rayleigh number Ra_f and decreases with the decrease in the Stefan number Ste. However, the time-averaged value of the global fluid fraction, i.e., \bar{F}_L , is seen to be independent of Ste; at $Ra_f = 3.96 \times 10^4$, the change in \bar{F}_L is limited to only 0.4% with five order change in

Ste. For $Ra_f = 3.96 \times 10^4$, the liquid domain has an average aspect ratio 0.72 (or $\bar{F}_L \approx 0.72$), and the next paragraph describes two kinds of flow configurations (configuration-P and configuration-Q) which exist for each Ste according to the time-averaged flow field results from the computer simulations (shown later in Sec. III B 1).

In Fig. 4(a), the curves for $Ste = 1.14 \times 10^{-2}$ and $Ste = 1.14 \times 10^0$ are with flow configuration-Q, while remaining three curves at $Ste = 1.14 \times 10^2$, 1.14×10^1 , and 1.14×10^{-1} are with flow configuration-P. Figure 5(b) shows the schematic diagram of phase-change Rayleigh-Bénard convection with configuration-P and configuration-Q. In configuration-P, the hot liquid shown by red color in Fig. 5(a) rises from the center of the box away from a wall and touches the solid-liquid interface and the cooler liquid shown by blue color sinks down along the opposite vertical wall and forms the primary convection cell (the largest cell inside the box). It should be noted that the central hot plume makes the solid-liquid interface approximately symmetric with a central hump. In configuration-Q, the hot liquid rises along a vertical wall, and the cooler liquid sinks near the center of the box away from the opposite vertical wall forming the primary convection cell [see Fig. 5(b)]. It should be noted that in configuration-Q (or configuration-P), there

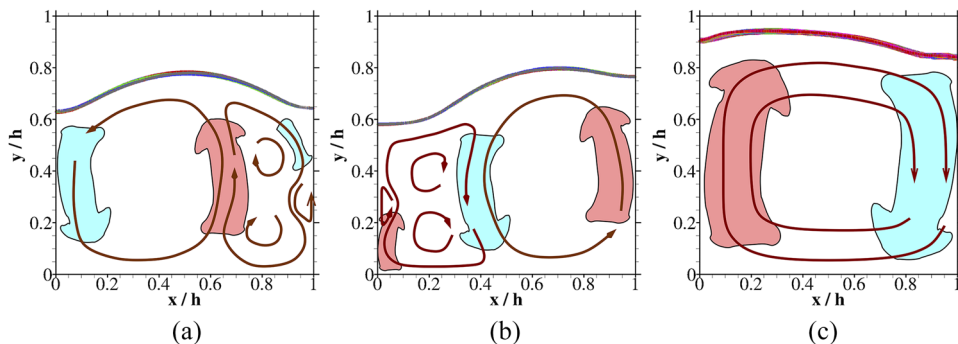


FIG. 5. The figure shows a schematic representation of different flow configurations in phase-change Rayleigh-Bénard convection (a) flow configuration-P at $Ra_f = 3.96 \times 10^4$, (b) flow configuration-Q at $Ra_f = 3.96 \times 10^4$, and (c) flow configuration for $Ra_f = 8.08 \times 10^6$. The brown lines show the circulation currents inside the flow structures, and blue and red arrows with mushroom-shaped cap show the location and flow direction of hot and cold plumes, respectively. Note that irrespective of Ra_f , the length scale of the large-scale fluid structures in the melt is of the order of the average height of the liquid domain or \bar{F}_L .

are two hot plumes (or two cold plumes) rising (or descending) from the vertical walls which merge together near the midline of the box to form a cold plume (or hot plume) after cooling (or heating) at the solid-liquid interface (or hot boundary). Repeated long-run stationary simulations were performed for three Stefan numbers ($\text{Ste} = 1.14 \times 10^0$, 1.14×10^{-1} , and 1.14×10^{-2} ; see Table I), and it was verified that both the configurations (P and Q) are possible at a given Ste at $\text{Ra}_f = 3.96 \times 10^4$; the selection of any configuration among configuration- P and configuration- Q is random in nature. At $\text{Ra}_f = 8.08 \times 10^6$, the liquid domain has an aspect ratio of 0.91, i.e., close to unity and the primary cell, based on the time-averaged flow field touches all the liquid domain boundaries [see Fig. 5(c)]. Irrespective of Ra_f , it is observed from the simulation results that flow structures are formed in such a way to fit a maximum number of cells of approximately unit cell-aspect-ratio, i.e., the average cell height is approximately equal to the averaged cell width. Therefore, it is observed that the length scale of the large-scale fluid structures in the melt is of the order of the average height of the liquid domain or \bar{F}_L . Thus, at higher Rayleigh number, only one flow configuration (with a primary cell touching all the boundaries) is observed for all the Stefan number.

B. Comparison of phase-change RB convection with classical RB convection

In this section, we report a detailed comparison of phase-change RB convection with the classical RB convection. Section III B reports the major similarities and differences of both the RB system for the time-averaged temperature field and flow field at different Ra_f (refer to Sec. III B 1), the effect of Rayleigh number Ra_f and Stefan number Ste on the wall-heat-flux and bulk kinetic energy (refer to Sec. III B 2), the effect of the Stefan number on the turbulent RB convection flow characteristics at the high Rayleigh number

(refer to Sec. III B 3) and finally, the scaling laws for both the RB systems involved for a wide range of Ste and Ra_f (refer to Sec. III B 4).

1. Effect of Ra_f on the time-averaged temperature and flow fields

Time-averaged temperature fields and velocity fields (in magnitude) along with the streamlines for the phase-change RB convection (at $\text{Ste} = 1.14 \times 10^{-1}$) and the equivalent classical RB convection are shown in Figs. 6 and 7 for different Ra_f . In both the phase-change and classical RB systems, the large-scale fluid motions are seen: the hot fluid rises upward, releases the heat at the cold boundary, and descends downward. It may be noted that the thermal boundary layers get thin and the bulk region homogenizes with the increase in Ra_f . The thermal plumes rise next to the side walls at high Ra_f and strengthen the large-scale convective motions. The increase in the circulation strength can be noted from the magnitude of velocity in the respective figures. Figure 8 (Multimedia view) shows the dynamic interaction between various cells for the equivalent classical RB system at $\text{Ra}_f = 3.96 \times 10^4$. There are two secondary clockwise rotating cells about half the height of the primary anticlockwise rotating cell placed one above the other, and these secondary cells attach and detach as seen in Fig. 8 (Multimedia view). In Fig. 7(d), the resultant time-averaged flow field shows that the top secondary cell attached to the bottom secondary cell and forms an elongated flow structure adjacent to the primary cell; such elongated flow structure comprising top and bottom secondary cells is also seen in Fig. 7(a) for the phase-change RB system. The time-averaged multicellular flow field for the equivalent classical RB systems is governed by Ra_f and the average aspect ratio of the liquid domain; however, for the phase-change RB system, it is additionally influenced by the curved oscillating solid-liquid interface that may also carry many or few, small or big undulations depending on the Ste and Ra_f [see the

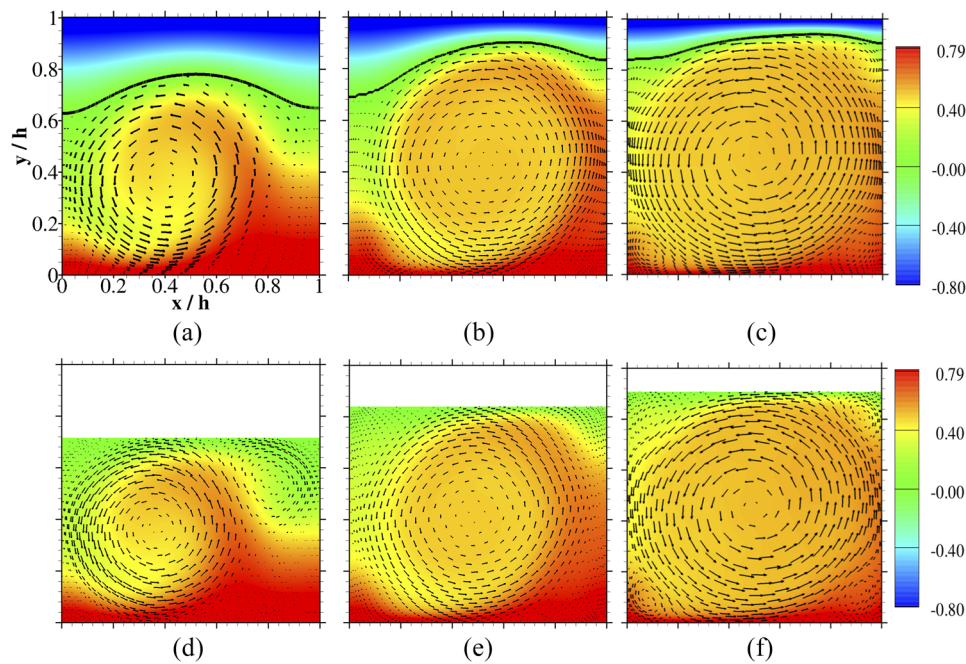


FIG. 6. Flood plots of time-averaged temperature overlapped with the time-averaged velocity vectors: Figs. 6(a)–6(c) for the phase-change RB system at $\text{Ste} = 1.14 \times 10^{-1}$ and Figs. 6(c)–6(f) for the equivalent classical RB system at three different Ra_f . Figures 6(a) and 6(d) at $\text{Ra}_f = 3.96 \times 10^4$, Figs. 6(b) and 6(e) at $\text{Ra}_f = 6.40 \times 10^5$, and Figs. 6(c) and 6(f) at $\text{Ra}_f = 8.08 \times 10^6$. Note that the x-axis and y-axis in all the above figures range from zero to one with a linear scale.

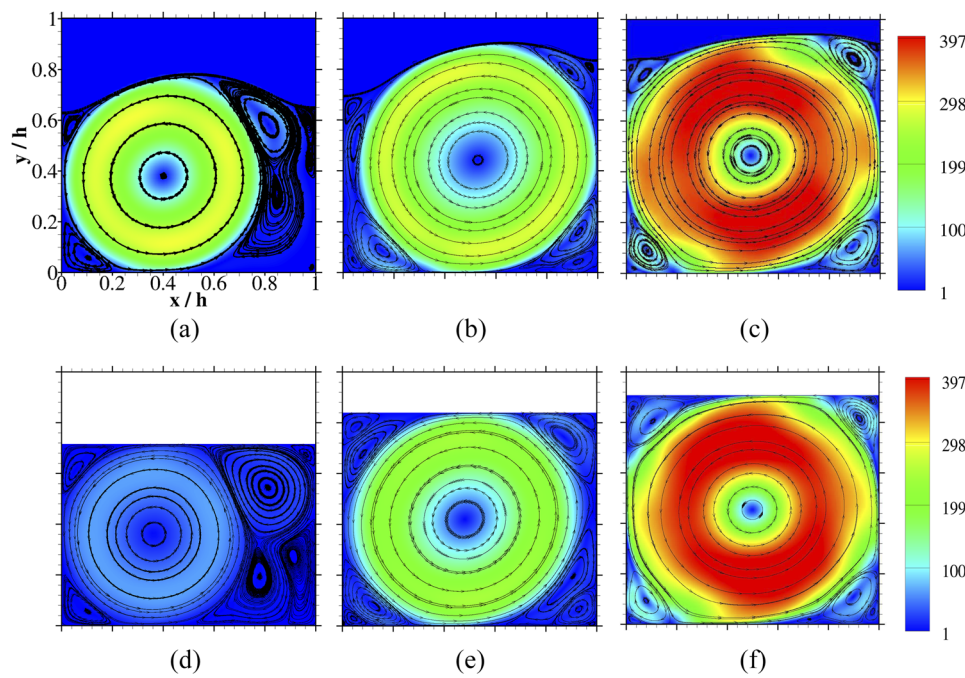


FIG. 7. Flood plots of time-averaged velocity magnitude ($|U|/U_0$) overlapped with the streamlines: Figs. 7(a)–7(c) for the phase-change RB system at $\text{Ste} = 1.14 \times 10^{-1}$ and Figs. 7(d)–7(f) for the equivalent classical RB system at three different Ra_f . Figures 7(a) and 7(d) at $Ra_f = 3.96 \times 10^4$, Figs. 7(b) and 7(e) at $Ra_f = 6.40 \times 10^5$, and Figs. 7(c) and 7(f) at $Ra_f = 8.08 \times 10^6$. Note that the x-axis and y-axis in all the above figures range from zero to one with a linear scale.

inset of Figs. 2(a), 2(b), 3(a), and 3(b)]. It should be noted that at low Ra_f except the primary cell, all other cells have relatively low velocities, the relative difference between the velocities of different cells is discussed later in Figs. 10(e) and 10(f).

Figure 9 shows the comparison of the time-averaged temperature field [see Figs. 9(a) and 9(b)] and time-averaged velocity field [see Figs. 9(c) and 9(d)] for flow configuration-P and flow configuration-Q obtained at $Ra_f = 3.96 \times 10^4$. In both the configurations, there is an annular region inside the primary cell where the convective currents are high. It is observed that the temperatures inside the primary cell for configuration-Q are relatively higher as

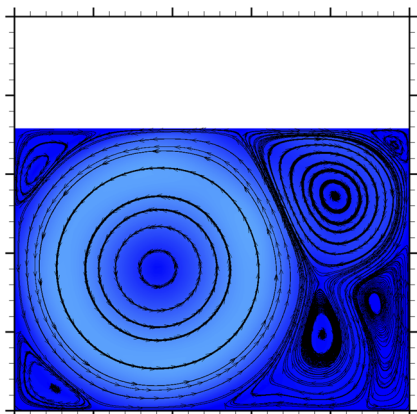


FIG. 8. Video shows the dynamic interaction between various cells for the equivalent classical RB system at $Ra_f = 3.96 \times 10^4$. Time-averaged velocity magnitude ($|U|/U_0$) contours overlaid with the streamlines for various non-dimensional time-steps τ are shown during the stationary state. Multimedia view: <https://doi.org/10.1063/1.5110295.1>

compared to the configuration-P. For the thermal configuration-P, it is seen that the hump of the solid-liquid interface is symmetric in the x-direction [see Fig. 6(a)], while for thermal configuration-Q, the hump of the solid-liquid interface is asymmetric in the x-direction.

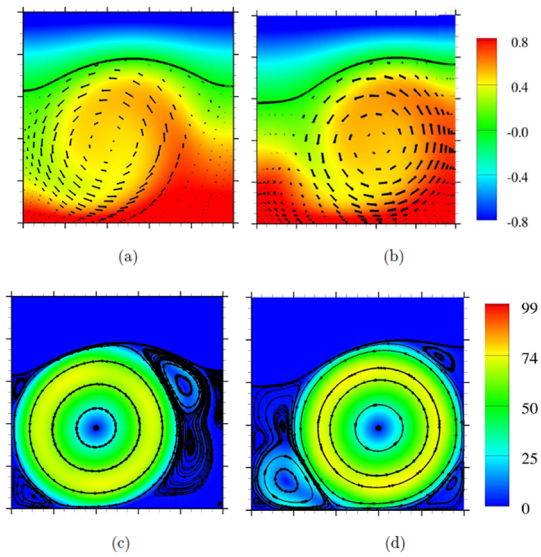


FIG. 9. Comparison of the time-averaged thermal field for flow configuration-P and flow configuration-Q obtained at $Ra_f = 3.96 \times 10^4$ and $\text{Ste} = 1.14 \times 10^{-1}$. The top panel shows the time-averaged temperature contours overlaid with the velocity vectors for both the flow configuration: (a) configuration-P and (b) configuration-Q. The bottom panel shows the time-averaged velocity magnitude ($|U|/U_0$) contours overlaid with the streamlines: (c) configuration-P and (d) configuration-Q. Note that the x-axis and y-axis in all the above figures ranges from zero to one with a linear scale.

This is because the location of the primary cell for configuration-Q has shifted to the right side and also the size of the primary cell is comparatively larger. It is observed in Figs. 9(c) and 9(d) that the size, shape, and convective strength of the top and bottom secondary cells in both the configurations are quite different. For configuration-P, the relatively stronger secondary cell is at the top, and a very weak secondary cell is at the bottom. On the contrary, for configuration-Q, the bottom secondary cell is relatively stronger, and the top secondary cell is very weak. Note that in both the thermal configurations (P and Q), the time-averaged global melt fraction \bar{F}_L is almost the same [see Figs. 4(a), 9(a), and 9(b)]. Later it will be shown that such small changes in thermal configurations can considerably modify the time-averaged wall heat flux and its fluctuations.

At $Ra_f = 3.96 \times 10^4$, the phase-change RB system has two prominent distinctions as compared to the equivalent classical RB system: (1) the top-cold-boundary for the phase-change RB system is curved as compared to the flat top-cold-boundary for the classical RB system and (2) the top-cold-boundary for the phase-change RB system is oscillating as compared to a rigid top-cold-boundary for the classical RB system. It is crucial to understand individually the effect of curved top-cold-boundary and effect of oscillating top-cold-boundary on the RB convection to thoroughly characterize the phase-change RB convection. Therefore, a new pure RB case is simulated at $Ra_f = 3.96 \times 10^4$ whose curved top-cold-boundary is a simplified version of the time-averaged curved top-cold-boundary for configuration-P [see Figs. 5(a) and 6(a)]. The small difference is that the solid-liquid interface for the case of the phase-change RB system shows two inflection points near the adiabatic vertical walls as it meets the vertical walls perpendicular to it. Henceforth, this new case will be identified as a curved pure RB case in this manuscript; the simulation grid for this case is shown in Appendix B (see the [supplementary material](#)). Figures 10(a) and 10(d) show the time-averaged temperature field and velocity field

for the curved pure RB system alongside the phase-change RB system with configuration-P [Figs. 10(b) and 10(e)] and the equivalent pure RB system with flat top-boundary [Figs. 10(c) and 10(f)] at $Ra_f = 3.96 \times 10^4$. The size of the primary cell and its convective strength for the curved pure RB case and phase-change RB case (with configuration-P) are quite similar but greater than that of the equivalent pure RB case [see Figs. 10(d)–10(f)]. Also, it is seen from Figs. 10(d)–10(f) that the magnitude of the velocities inside the top secondary cell is relatively higher for the equivalent pure RB case as compared to that of the curved pure RB case and phase-change RB case with configuration-P.

Figures 11(a)–11(c) show the horizontally and time-averaged temperature profiles and magnitude of velocity profiles inside the box for the pure RB system, curved pure RB system, and phase-change RB system with configuration-P and configuration-Q at $Ra_f = 3.96 \times 10^4$. It can be seen from Figs. 11(a) and 11(b) that all the horizontally and time-averaged temperature profiles for different RB systems show a high-temperature gradient at hot and cold boundary layer and a weakly stratified central zone inside the box. Although, the pure RB system, curved RB system, and phase-change RB system with configuration-P and configuration-Q have only minor differences in the horizontally and time-averaged temperature profiles but show considerable differences in the horizontally and time-averaged magnitude of velocity profiles for all the four cases shown in Fig. 11(c). It should be noted that the horizontally averaged and time-averaged magnitude of velocity profiles are not shown in the region where the top boundary or solid-liquid interface is curved. We neglect the aforementioned region because this region is highly dynamic in space and time due to the constant phase-change events, and the velocities suddenly change from zero in the solid-phase to a high positive value in the liquid region. The peak velocity in the bottom half of the box is least for the pure RB case; configuration-P and curved pure RB are $\approx 22\%$ higher, and configuration-Q is 38% higher than the peak velocity of the pure RB case. The minimum

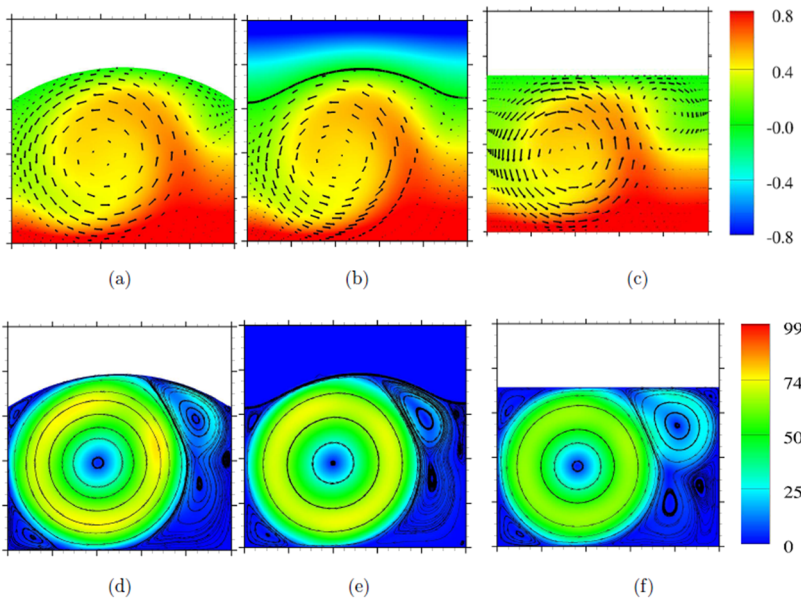


FIG. 10. The left column [Figs. 10(a) and 10(d)], middle column [Figs. 10(b) and 10(e)], and the last column [Figs. 10(c) and 10(f)] show the time-averaged temperature field (top panel) and the velocity field (bottom panel) for the curved pure RB case, phase-change RB system with configuration-P, and equivalent pure RB system with flat top-boundary, respectively, at $Ra_f = 3.96 \times 10^4$. Note that the shape and size of the top-cold-boundary for the curved pure RB case are almost identical to the shape and size of the time-averaged solid-liquid interface for configuration-P obtained for the phase-change RB system at $Ra_f = 3.96 \times 10^4$.

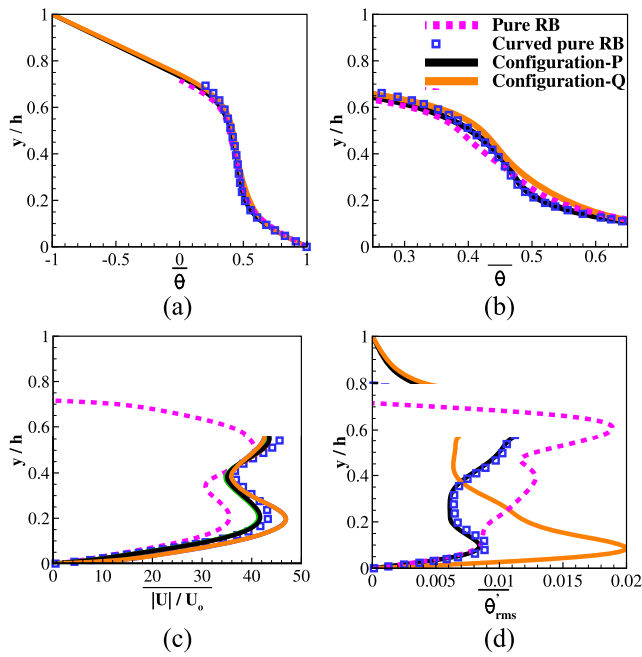


FIG. 11. Comparison of horizontally and time-averaged thermal characteristics for the phase-change RB system and classical RB system (different color continuous lines shown for configuration-*P* and configuration-*Q*) and the classical RB system (shown by dotted pink line) at $Ra_f = 3.96 \times 10^4$: (a) $\bar{\theta}$ vs y/h , (b) zoomed $\bar{\theta}$ vs y/h , (c) magnitude of velocity $|U|/U_0$ vs y/h , and (d) $\bar{\theta}_{rms}$ vs y/h . Note that in the region near the curved top boundary (or solid-liquid interface for the phase-change RB system), the horizontal averaging of the time-averaged data is not useful and thus not shown in the above plots.

velocities in the central region of the box are almost same for the curved pure RB system and phase-change RB system with configuration-*P* and configuration-*Q* but greater than the minimum velocity for the pure RB system. The pure RB system is having the least time-averaged values of the Nusselt number (see Table I and Sec. III B 2) among all the RB systems at $Ra_f = 3.96 \times 10^4$ because it has lower magnitudes of velocity throughout the box. All the RB systems at $Ra_f = 3.96 \times 10^4$ have an aspect ratio of 0.72, and the flow inside the box shows unsteady laminar RB convection [shown later in Fig. 12(a)]; the top and bottom secondary cells undergo maximum oscillations [see Fig. 8 (Multimedia view) and Fig. 10(f) for pure RB case]. It is observed from Fig. 11(d) that the values of the

time-averaged and horizontally averaged root-mean-square value of the temperature fluctuation $\bar{\theta}_{rms}$ in the bottom half of the RB box is the highest for the phase change RB system with configuration-*Q* and it is more than twice that of configuration-*P*, curved pure RB, and pure RB; here, the temperature fluctuation at a grid-point is defined as $\theta' = \theta - \bar{\theta}$ for calculation of the root-mean-square value. Similarly, the fluctuations of the temperature are highest in the upper half of the RB box for the pure RB system. This is because the strongest secondary cell is located near the bottom for the phase-change RB system with configuration-*Q* [see Fig. 9(d)] and at the top for the pure RB system [see Fig. 10(f)]. This can be correlated with the fluctuation of the Nusselt number at the bottom of the RB box at $Ra_f = 3.96 \times 10^4$ in Sec. III B 2.

Energy spectra computed using the Fourier transforms of the vertical velocity signal taken at the midpoint of the box are shown in Fig. 12 for the phase-change Rayleigh–Bénard convection system with configuration-*P* at $Ste = 1.14 \times 10^{-1}$, the curved pure RB system (shown only at low Ra_f), and the equivalent pure/classical RB system at three different Rayleigh numbers. At the low Rayleigh number $Ra_f = 3.96 \times 10^4$, a unique peak with a maximum value of energy and couple of small peaks in the frequency power spectrum are seen in Fig. 12(a) for all the three RB systems depicting that the flow inside the box is unsteady and laminar. It should be noted that the strongest peak frequency for the case of the phase-change RB system is almost double than the strongest peak frequency for the pure RB system and equal to that of the curved pure RB system. The enhancement in the dominant RB convection frequency for the phase-change RB system with configuration-*P* may be due to the curved shape of the solid-liquid interface. For both the RB systems, the energy spectra show a periodic signal with a couple of dominant peaks (unsteady laminar) at low Ra_f and a broadband signal (possibly turbulent) at high Ra_f ; while a transition is seen in Fig. 12(b).

2. Effect of Ra_f and Ste on wall-heat-flux and bulk kinetic energy

In the last section, the flow field and temperature field at different Ra_f were compared for both the equivalent classical RB system and phase-change RB system. In this section, the effect of Ste and Ra_f on the time-averaged Nusselt number at the hot plate \bar{Nu}_h , one standard deviation of Nu_h , and the bulk kinetic energy during the stationary state is reported for the phase-change RB system and compare it with the respective quantities for the equivalent classical RB system.

Figure 13(a) shows the comparison of the Nusselt number Nu_h at the hot wall vs modified nondimensional time $\tau - \tau_s$ for the

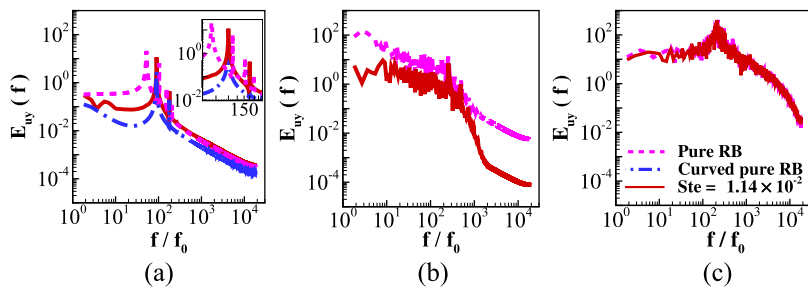


FIG. 12. Frequency power spectrum of vertical velocity component (U_y/U_0) at the mid-point ($x/h = 0.5$) and ($y/h = 0.5$) for the pure/classical Rayleigh Bénard convection system (shown with red continuous line), the curved pure RB system (shown with dot-dash-dot blue line only at low Ra_f), and the phase-change Rayleigh Bénard convection system with configuration-*P* (shown with pink colored dotted line) at different Rayleigh numbers: (a) $Ra_f = 3.96 \times 10^4$, (b) $Ra_f = 6.40 \times 10^5$, and (c) $Ra_f = 8.08 \times 10^6$.

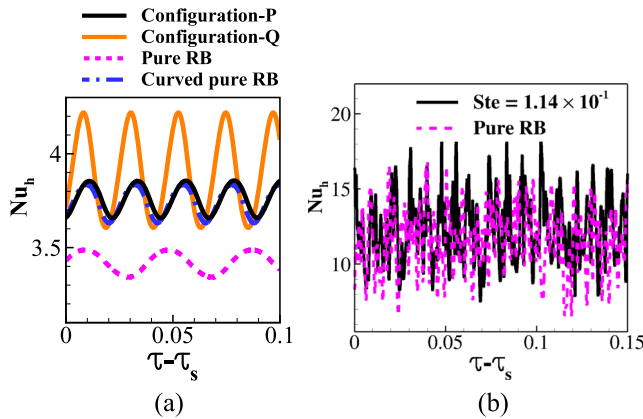


FIG. 13. Oscillatory nondimensional wall heat flux at the hot wall Nu_h plotted vs the modified nondimensional time $\tau - \tau_s$ at different Rayleigh numbers: (a) $Ra_f = 3.96 \times 10^4$ and (b) $Ra_f = 8.08 \times 10^6$.

phase-change RB system, the curved pure RB system, and the classical RB system at $Ra_f = 3.96 \times 10^4$. At $Ra_f = 3.96 \times 10^4$, it is seen that the time-averaged value of Nu_h for flow configuration-Q is the highest, while \bar{Nu}_h is lowest for the classical RB system; \bar{Nu}_h for flow configuration-P and the curved pure RB system are almost the same as they have a very similar curved boundary. This trend in the values of \bar{Nu}_h for different cases matches with the trend of the horizontal and time-averaged magnitude of the velocity $\overline{|U|}/U_o$ near the hot plate seen in Fig. 11(c) as the heat transport is primarily due to convection. At $Ra_f = 8.08 \times 10^6$, it is seen in Fig. 13(b) that the signal Nu_h vs $\tau - \tau_s$ for both the phase-change RB system and the classical RB system is irregular, and the peak values of Nu_h are often higher for the case of the phase-change RB system.

Figure 14(a) shows the time-averaged Nusselt number computed at the hot wall as a function of the Stefan number for $Ra_f = 3.96 \times 10^4$, $Ra_f = 6.40 \times 10^5$, and $Ra_f = 8.08 \times 10^6$ for the phase-change RB system. As expected, \bar{Nu}_h increases with the increase in the Rayleigh number [see Fig. 14(a)] as the thermal and velocity boundary layers become thinner. At low Ra_f , the time-averaged value of the Nusselt number \bar{Nu}_h is independent of the Stefan number Ste ; it is seen in Fig. 14 that \bar{Nu}_h for group-Q (exhibiting configuration-Q; $\bar{Nu}_h \approx 3.9$) is 4% higher than that for group-P (exhibiting configuration-P; $\bar{Nu}_h \approx 3.76$). For $Ra_f = 6.40 \times 10^5$, the time-averaged Nusselt number is weakly dependent on the Stefan number. However, at $Ra_f = 8.08 \times 10^6$, with a reduction in Ste by five orders (approximately from 10^2 to 10^{-2}), \bar{Nu}_h is enhanced by 10.9% (from 11.54 to 12.80).

Here, we try to answer an important question—“does the phase-change RB system have a better heat transfer performance as compared to the classical RB system?” Figure 14(b) shows the plot of $\bar{Nu}_h/\bar{Nu}_h^{RB}$ vs the Stefan number, where $\bar{Nu}_h/\bar{Nu}_h^{RB}$ is the ratio of the time-averaged Nusselt number at the hot wall for the phase-change RB system to that of the classical RB system at the stationary state. Among all the cases, the highest value of $\bar{Nu}_h/\bar{Nu}_h^{RB}$ is seen for the group-Q (exhibiting configuration-Q) at $Ra_f = 3.96 \times 10^4$. At

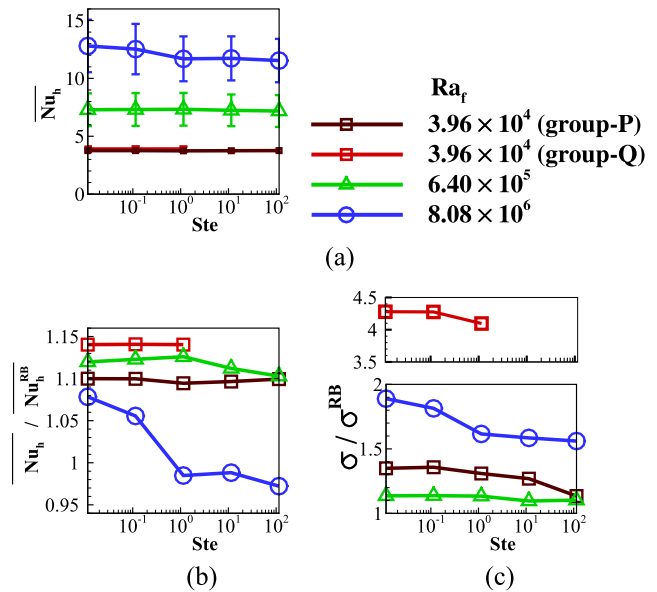


FIG. 14. Effect of the Stefan number Ste at three different Rayleigh numbers on the heat transport statistics at the hot wall during the stationary state: (a) \bar{Nu}_h vs Ste , (b) $\bar{Nu}_h/\bar{Nu}_h^{RB}$ vs Ste , and (c) σ/σ^{RB} vs Ste .

$Ra_f = 3.96 \times 10^4$, the Nusselt number at the hot wall for the case of phase-change RB system is enhanced by $\approx 10\%$ and $\approx 14\%$ for the group-P and group-Q, respectively, as compared to the classical RB system. The enhanced heat transport for the phase-change RB system as compared to the equivalent classical RB system is because of the curved solid-liquid interface, which can accommodate a bigger cell (see Fig. 10). The bigger cell has relatively higher buoyancy forces as its cell-based Rayleigh number is higher as compared to the equivalent classical RB system, which has a flat cold boundary. Note that both the RB systems have the same Ra_f and the same average liquid aspect ratio $\frac{hy}{h}$. For $Ra_f = 6.40 \times 10^5$, the ratio $\bar{Nu}_h/\bar{Nu}_h^{RB}$ is a weak function of Ste ; the Nusselt number at the hot wall for the case of the phase-change RB system is enhanced by 10.29%–12.59% as compared to the classical RB system. It is seen from Fig. 14(b) that the value of $\bar{Nu}_h/\bar{Nu}_h^{RB}$ reduces with the increase in Ra_f , and earlier it was shown in Figs. 6 and 7 that the average or bulk radius of curvature of the solid-liquid interface increases, or the time-averaged solid-liquid interface tends to become relatively flatter with the increase in the Rayleigh number Ra_f . Apart from this at $Ra_f = 8.08 \times 10^6$, for $Ste > 1.14$, with the increase in Ste by one and two orders, it is observed that the Nusselt number at the hot wall for the case of the phase-change RB system decreases by 1.18%–2.79%, respectively, as compared to the classical RB system. However, for $Ste < 1.14$, it is observed that the Nusselt number at the hot wall for the case of the phase-change RB system at $Ste = 1.14 \times 10^{-1}$, 1.14×10^{-2} is enhanced by 5.56%–7.83%, respectively, as compared to the classical RB system. This enhancement (or decrement) in \bar{Nu}_h for $Ste < 1.14$ (or $Ste > 1.14$) with respect to \bar{Nu}_h^{RB} is due to the absence (or presence) of small undulations on the solid-liquid interface which interfere with the bulk convective motion to increase (or reduce) its

strength according to Fig. 15(b) (detailed explanation provided in Sec. III B 3).

The error bar shown in Fig. 14(a) represents σ one standard deviation from the time-averaged value of Nu_h . Figure 14(c) shows the ratio σ/σ^{RB} , where σ and σ^{RB} are the value of one standard deviation of the Nusselt number at the hot wall for the phase-change RB system and equivalent pure RB system, respectively. σ^{RB} increases with Ra_f (see Table I for details), and σ is always greater than σ^{RB} . At a given Ra_f , σ is always greater than σ^{RB} because the oscillating curved solid-liquid interface results in a more fluctuating flow field in order to accommodate the dynamic changes in the volume of the RB domain. The fluctuations of Nu_h as compared to that of the equivalent pure RB case are more pronounced in the turbulent regime (see discussion to Fig. 12). Furthermore, it is seen that σ (or σ/σ^{RB}) at all Ra_f increases with Ste (see Table I for details). At $Ra_f = 3.96 \times 10^4$, the values of σ primarily depend on the flow configuration. At $Ste = 1.14$ and $Ra_f = 3.96 \times 10^4$, the value of σ/σ^{RB} increases by $\approx 68\%$ ($\sigma_p/\sigma^{RB} = 4.096$ and $\sigma_Q/\sigma^{RB} = 1.308$). The values of the standard deviation of the Nusselt number at the hot wall for configuration-P and configuration-Q are well correlated with the time-averaged and horizontally averaged temperature fluctuations $\overline{\theta'_{rms}}$ vs y/h shown in Fig. 11(d).

Figures 15(a) and 15(b) show the plot of volume-averaged total kinetic energy $U_T^2 = (\frac{1}{V} \oint_V U_x^2 + U_y^2 dV)$ vs the nondimensional time, normalized with the square of the thermal diffusion speed [$U_0^2 = (\alpha_{th}/h)^2$] at $Ra_f = 3.96 \times 10^4$ and $Ra_f = 8.08 \times 10^6$ for the phase-change RB system, the curved pure RB system [shown only in Fig. 15(a) for $Ra_f = 3.96 \times 10^4$], and the classical RB system. In Fig. 15(a) at $Ra_f = 3.96 \times 10^4$, the total kinetic energy $\overline{U_T^2}$ fluctuates at some distinct frequencies due to the unsteady laminar convection; however, among all the four curves shown in Fig. 15(a), the equivalent pure RB case has the least value of time-averaged and volume-averaged total kinetic energy $\overline{U_T^2}$; the value of $\overline{U_T^2}$ for configurations-Q of the phase-change RB system, curved pure RB system, and configurations-P of the phase-change RB system is 48.64%, 43.91%, 35.81% higher than the value of $\overline{U_T^2}$ for the equivalent pure RB

system, respectively. The results are consistent with the time-averaged velocity fields shown in Figs. 9 and 10 and as explained earlier the enhancement of $\overline{U_T^2}$ is due to the curved-cold-boundary (at $\theta = 0.5$) which have a larger length ($l_p > h$) and the curved-cold-boundary facilitate the formation of primary cell of a relatively higher height for the case of the phase-change RB system and curved pure RB system. Figure 15(b) shows relatively higher values of $\overline{U_T^2}$ at the low Stefan number case as compared to the high Stefan number case. Also, as expected at $Ra_f = 8.08 \times 10^6$, the value of $\overline{U_T^2}$ and its fluctuations in time during the stationary state are higher as compared to the respective values at $Ra_f = 3.96 \times 10^4$ [see Figs. 15(a) and 15(b)].

3. Effect of Ste on the turbulent RB convection flow characteristics at high Ra_f

In Secs. II and III, it was seen that at the high Rayleigh number ($Ra_f \geq 8.08 \times 10^6$), the heat transport characteristics are highly dependent on the Stefan number (see Sec. III B 2 and Table I) and $\overline{Nu_h}/\overline{Nu_h}^{RB}$ can be less than or greater than unity. To understand this, in this section, we first study the flow dynamics during the stationary state for the low Stefan number phase-change RB system, high Stefan phase-change RB system, and the equivalent RB system at $Ra_f = 8.08 \times 10^6$. Later the effect of the Stefan number on the time-averaged and horizontally averaged temperature and velocity magnitude profiles, root-mean-square values of the temperature fluctuation, and turbulent kinetic energy profiles are studied for the phase-change RB system. Finally, in this section, the effect of the Stefan number on the strength of the solid-liquid interface oscillations is reported.

At $Ra_f = 3.96 \times 10^4$, the curvature and the form of the solid-liquid interface are almost constant during the stationary state (refer to Fig. 2) as the flow field has very small vertical oscillations [refer to Fig. 16 (Multimedia view)].

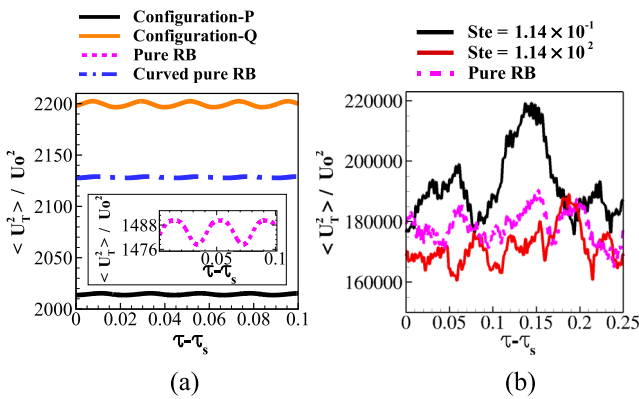


FIG. 15. Oscillatory volume-averaged total kinetic energy ($U_T^2 = \frac{1}{V} \oint_V U_x^2 + U_y^2 dV$) vs the nondimensional time $\tau - \tau_s$, normalized with the square of speed of thermal diffusion [$U_0^2 = (\alpha_{th}/h)^2$] at two different Rayleigh numbers: (a) at $Ra_f = 3.96 \times 10^4$ and (b) at $Ra_f = 8.08 \times 10^6$.

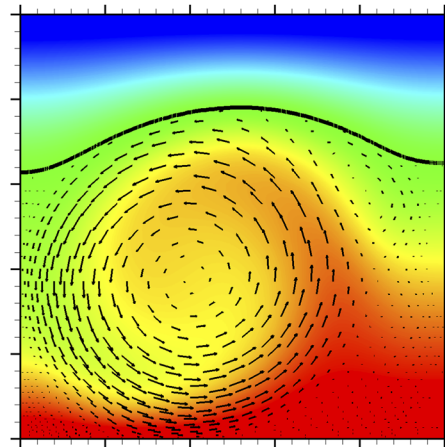


FIG. 16. Video shows the time evolution of the large scale dynamics for $Ste = 1.14 \times 10^{-1}$ at $Ra_f = 3.96 \times 10^4$. Dimensionless temperature contours $\theta = (T - T_m)/(T_h - T_m)$ are overlaid with the dimensionless velocity vectors at the midplane of the box for different nondimensional times τ . Multimedia view: <https://doi.org/10.1063/1.5110295.2>

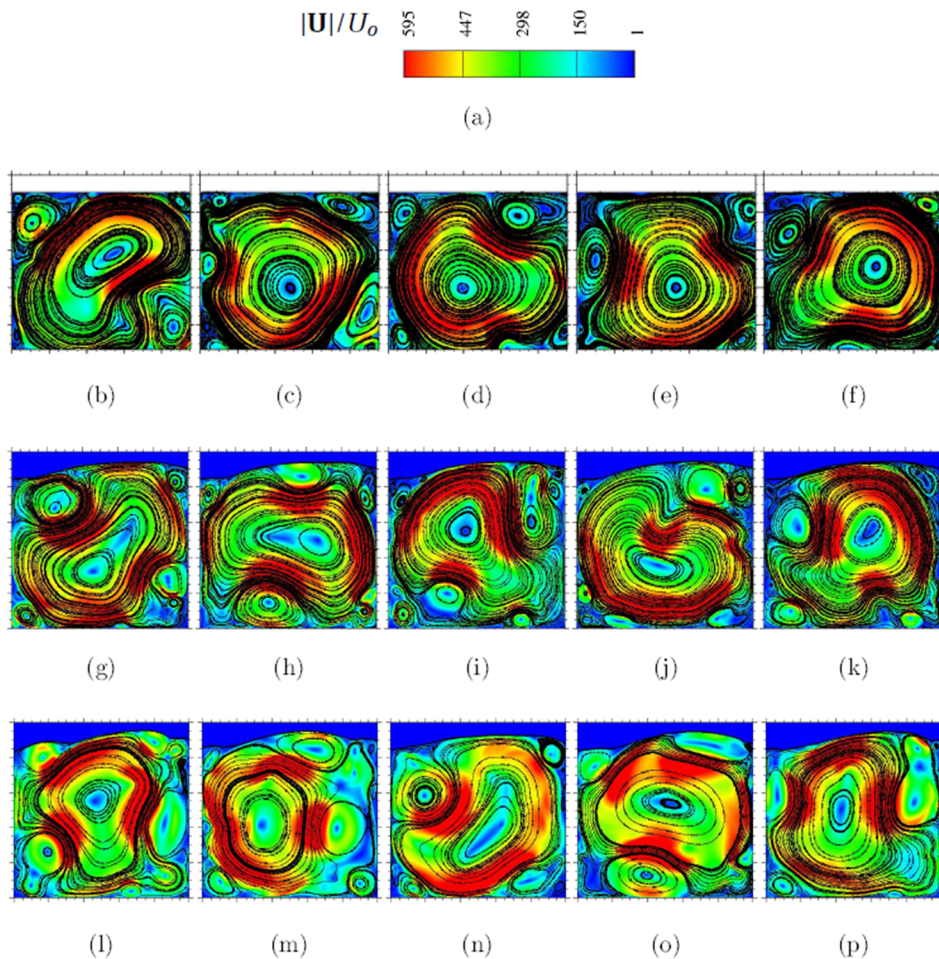


FIG. 17. Flood plots of dimensionless velocity magnitude ($|U|/U_0$) overlapped with the streamlines at $Ra_f = 8.08 \times 10^6$ for the phase-change RB system and equivalent pure RB system. Figure 17(a) shows the scalebar for $|U|/U_0$. The black line represents the solid-liquid interface. A comparison of the large-scale flow dynamics at five consecutive time instants (with $\Delta\tau = 2 \times t_0$) during the stationary state for the pure RB system and phase-change system: Figs. 17(b)–17(f) for pure RB, Figs. 17(g)–17(k) for the low Stefan number phase-change RB system with $\text{Ste} = 1.14 \times 10^{-1}$, and Figs. 17(l)–17(p) for the high Stefan number phase-change RB system with $\text{Ste} = 1.14 \times 10^2$. Note that the x-axis and y-axis in all the above figures range from zero to one with a linear scale.

Figure 17 shows the velocity field for the pure RB system and the phase-change systems at five consecutive time instants (with $\Delta\tau = 2 \times t_0$) during the stationary state at $Ra_f = 8.08 \times 10^6$. In all the cases, the primary cell is always rotating in the anticlockwise direction, and its immediate neighboring cells are rotating in the clockwise direction. At $Ra_f = 8.08 \times 10^6$, the flow field is highly unsteady, especially due to the chaotic spatio-temporal plume dynamics. The form of the curved solid-liquid interface for the low Stefan number case at $\text{Ste} = 1.14 \times 10^{-1}$ [see Figs. 17(g)–17(k)] undergoes almost no change with time, while it is seen to drastically change for the high Stefan number case at $\text{Ste} = 1.14 \times 10^2$ [see Figs. 17(l)–17(p)]. Note that the multiple inflection points on the solid-liquid interface are seen in Figs. 17(l)–17(p), where locally the concave surface changes to the convex surface. It is observed that the values of the peak velocity zones appearing on the periphery of the primary cell (see Fig. 17) for the case of the high Stefan number ($\text{Ste} = 1.14 \times 10^2$) are slightly less than the low Stefan number case ($\text{Ste} = 1.14 \times 10^{-1}$) and the pure RB case. These results are consistent with the earlier results discussed in Fig. 15(b). It appears that the increased number in inflection points on the oscillating solid-liquid interface for the high Stefan number

case at $\text{Ste} = 1.14 \times 10^2$ are slightly detrimental for the bulk flow field.

The time-averaged and horizontally averaged temperature and velocity magnitude profiles inside the RB box are shown for both the phase-change and classical RB systems in Fig. 18. The zoomed plot of the time-averaged and horizontally averaged temperature profile in Fig. 18(b) shows that the time-averaged and horizontally averaged core temperature for the case with $\text{Ste} = 1.14 \times 10^2$ and the case of the pure RB system is 4% and 2% higher than the case with $\text{Ste} = 1.14 \times 10^{-1}$. Note that with respect to the pure RB system, the phase-change RB shows two different regimes due to two different kinds of solid-liquid interface oscillation patterns—for $\text{Ste} \leq 1$ [see the description of Figs. 17(g)–17(k)] and for $\text{Ste} > 1$ [see the description of Figs. 17(l)–17(p)]. Similarly, Fig. 18(c) shows that the horizontally and time-averaged velocity magnitude for $\text{Ste} = 1.14 \times 10^{-1}$ (and $\text{Ste} = 1.14 \times 10^2$) is more (less) than the pure RB case.

Figure 19 shows the comparison of the time-averaged and horizontally averaged root-mean-square values of the temperature fluctuation $\overline{\theta'^2_{rms}}$ and turbulent kinetic energy TKE profiles inside the box for both the phase-change and classical RB systems at $Ra_f = 8.08 \times 10^6$. The inset in Fig. 19(a) shows that the peak values

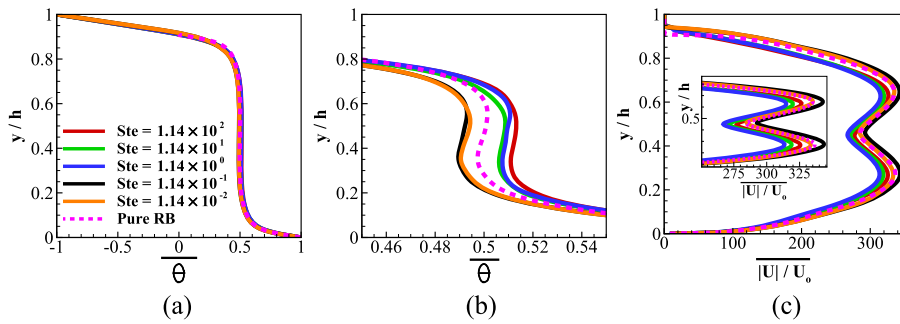


FIG. 18. Comparison of horizontally and time-averaged thermal characteristics for the phase-change RB system and classical RB system (different color continuous lines shown for different values of Ste) and classical RB system (shown by dotted pink line) at $Ra_f = 8.08 \times 10^6$: (a) $\bar{\theta}$ vs y/h , (b) zoomed $\bar{\theta}$ vs y/h , and (c) magnitude of velocity $|U|/U_o$ vs y/h .

of the time-averaged and horizontally averaged temperature fluctuations $\overline{\theta'_{rms}}$ inside the thermal boundary layer near the hot wall for the case of the phase-change RB system with $Ste = 1.14 \times 10^2$ is less than all other cases of the phase-change RB system and pure RB case; also, it should be noted that there is a monotonic rise in the peak values of the time-averaged and horizontally averaged temperature fluctuations $\overline{\theta'_{rms}}$ with the decrease in Ste. We neglect the horizontally averaged results very close to the time-averaged position of solid-liquid interface $y/h \sim 0.91$ where the solid-liquid interface fluctuates (see Fig. 3), and there is a transition from the solid to liquid or liquid to solid phase. This is because the order of $\overline{\theta'_{rms}}$ changes significantly in solid and liquid regions and horizontal averaging in such a region which is not only curved, but dynamic in time and space may lead to erroneous interpretations. It is clear from the time-averaged and horizontally averaged turbulent kinetic energy profiles in Fig. 19(b) that the peak values of TKE for all cases of the phase-change RB system are higher than that of the pure RB system; also note that the peak values in the time-averaged and horizontally averaged turbulent kinetic energy profile do not monotonically vary with Ste. The time-averaged and horizontally averaged turbulent heat flux is proportional to the product the time-averaged and horizontally averaged temperature fluctuations $\overline{\theta'_{rms}}$ and turbulent kinetic energy TKE. For the low Stefan number ($Ste < 1$) phase-change RB system, both time-averaged and horizontally averaged velocity and turbulent

kinetic energy values are higher as compared to the high Stefan number ($Ste > 1$) phase-change RB system and pure RB system which are well correlated with the heat transfer performance for the respective RB systems.

Figure 20 shows the power spectra for the global melt fraction for five different Ste at $Ra_f = 3.96 \times 10^4$ [Fig. 20(a)] and $Ra_f = 8.08 \times 10^6$ [Fig. 20(b)]. For easy comparison, all the five curves in Figs. 20(a) and 20(b) are separately shown in Figs. C1(a) and C1(b) in Appendix C (see the [supplementary material](#)). The magnitude of the fluctuations of the global melt fraction indicates the volume of the substance undergoing phase-change and is correlated with the movement (or the strength of oscillations) of the solid-liquid interface about a mean position as shown in Figs. 2–4. The power $E_{F_L}(f)$ in Fig. 20 depicts the strength of F_L vs time signal (see Fig. 4) for different frequencies shown in the frequency power spectrum. Figure 20 shows that at higher frequencies, the power $E_{F_L}(f)$ is relatively small which means that the high-frequency phase-change events are related to the small undulations on the solid-liquid interface, i.e., the amount of the volume undergoing the phase-change events is small. It is observed that the power $E_{F_L}(f)$ or the intensity of the fluctuation of the solid-liquid interface increases with the increase in the Rayleigh number from 3.96×10^4 to 8.08×10^6 . The fluctuation of the solid-liquid interface or the power $E_{F_L}(f)$ and the spectrum bandwidth is expected to increase with the increase in the circulation strength and with the increase in the turbulence intensity of the buoyancy-driven flow at the high Rayleigh number. The power $E_{F_L}(f)$ for the entire frequency band monotonically decreases with the decrease in the Stefan number at $Ra_f = 3.96 \times 10^4$. However, at $Ra_f = 8.08 \times 10^6$, the decrease in $E_{F_L}(f)$ for all the frequencies in the frequency power spectrum [shown in Fig. 20(b)] is seen only at low Stefan numbers (i.e., for $1.14 \times 10^{-2} \leq Ste \leq 1.14 \times 10^{-1}$). This nonmonotonic decrease in $E_{F_L}(f)$ at all the frequencies in the frequency power spectrum for $Ste > 1$ is again associated with two different kinds of the solid-liquid interface oscillations pattern—for $Ste \leq 1$ [see the description of Figs. 17(g)–17(k)] and for $Ste > 1$ [see the description of Figs. 17(l)–17(p)]. Although this section deals with only high Ra_f , the power spectrum for the global melt fraction at low Ra_f is described here to highlight that two different kinds of solid-liquid interface oscillation pattern are observed only at higher Ra_f .

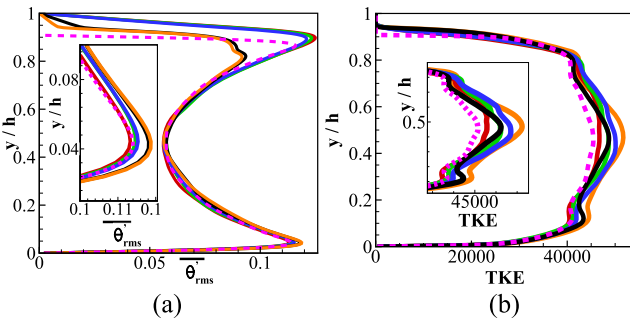


FIG. 19. Effect of Ste on the time-averaged and horizontally averaged turbulent quantities at $Ra_f = 8.08 \times 10^6$: (a) $\overline{\theta'_{rms}}$ profiles inside the box and (b) turbulent kinetic energy TKE profiles inside the box. The different colored continuous lines are used to plot the respective quantities for the phase-change RB systems, while the dashed pink line is used for the classical RB system; legends for both the left and right subfigures are same as specified in Fig. 18(a).

4. Scaling laws for phase-change RB convection

Figure 21 shows the average aspect ratio of the RB box or time-averaged global liquid volume fraction $\overline{F_L}$ at the stationary state for

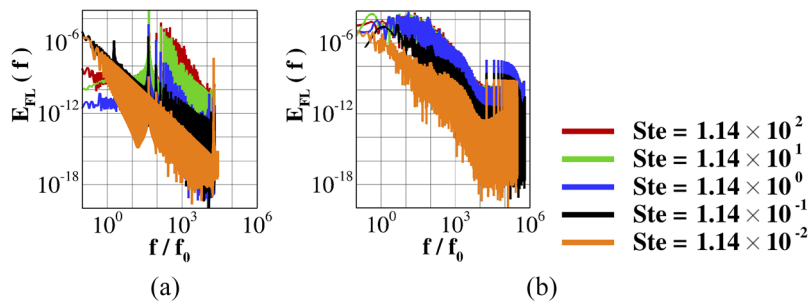


FIG. 20. Frequency power spectrum of global melt fractions (F_L) for five different Ste for the phase-change RB system at different Rayleigh numbers: (a) $\text{Ra}_f = 3.96 \times 10^4$ and (b) $\text{Ra}_f = 8.08 \times 10^6$.

different Ra_f . It is seen that $\overline{F_L}$ increases with the increase in Ra_f ; and at higher Ra_f , $\overline{F_L}$ starts to approach a value of unity. Figure 22 shows the scaling laws for the time-averaged Nusselt number at the hot wall for both the phase-change and classical RB systems vs the Rayleigh number based on the fluid height Ra_f . All the scaling laws proposed here are for the studied range of Ra_f ($3.96 \times 10^4 \leq \text{Ra}_f \leq 9.26 \times 10^7$). The Nusselt number, for all the shown cases, is seen to increase with Ra_f and the best fit shows a power-law scaling $\overline{\text{Nu}}_h^{\text{RB}} \propto \text{Ra}_f^{0.2358}$ for the classical RB system, $\overline{\text{Nu}}_h \propto \text{Ra}_f^{0.2221}$ (at $\text{Ste} = 1.14 \times 10^{-1}$) and $\overline{\text{Nu}}_h \propto \text{Ra}_f^{0.2131}$ (at $\text{Ste} = 1.14 \times 10^2$) for the phase-change RB system. It is seen that for the laminar flow regime at lower Ra_f , $\overline{\text{Nu}}_h$ for the phase-change system (configuration-P) is higher than the pure RB system because the curvature of the top interface in the phase change system enhances Rayleigh–Bénard convection; also, the configuration-Q (not shown in figure) further enhances the RB convection compared to configuration-P. For the turbulent flow regime at higher Ra_f , $\overline{\text{Nu}}_h$ for the pure RB system increases crosses $\overline{\text{Nu}}_h$ for the phase-change system with high Ste and finally approaches the phase-change RB system for low Ste because the solid-liquid interface becomes relatively flatter at higher Ra_f . It should also be noted that for $\text{Ra}_f \geq 8.08 \times 10^6$, $\overline{\text{Nu}}_h$ at $\text{Ste} = 1.14 \times 10^2$ is always less than the pure RB system because the form of the curvature is not stable throughout the stationary state. Similarly, for $\text{Ra}_f \geq \text{Ra}_f = 8.08 \times 10^6$, $\overline{\text{Nu}}_h$ at $\text{Ste} = 1.14 \times 10^{-1}$ is always more

than the pure RB system because the form of the curvature is stable throughout the stationary state. The exponent of Ra_f for the classical RB system is 9.62% and 6.17% higher as compared to the high Stefan number case (at $\text{Ste} = 1.14 \times 10^2$) and at the low Stefan number case (at $\text{Ste} = 1.14 \times 10^{-1}$) of the phase-change RB system, respectively. For $\text{Ra}_f \geq 8.08 \times 10^6$, in the turbulent flow regime, the difference in the value of $\overline{\text{Nu}}_h$ for the high Stefan number case (at $\text{Ste} = 1.14 \times 10^2$) and at the low Stefan number case (at $\text{Ste} = 1.14 \times 10^{-1}$) reduces with the increase in Ra_f and the values of $\overline{\text{Nu}}_h$ for the phase-change system are very close to the pure RB system (see Table I) this is because at the higher Rayleigh number ($\text{Ra}_f = 9.26 \times 10^7$), the solid-liquid interface is very close to top boundary ($F_L = 0.95$), subjected to high-temperature gradients which restrict the fluctuations of the solid-liquid interface. Also, note that many earlier classical RB convection experimental and numerical studies for the low Prandtl number fluid ($\text{Pr} = 0.0216$) have suggested a power-law $\overline{\text{Nu}}_h \propto \text{Ra}_f^\beta$, and the value of exponent β ranges from 0.25 to 0.26 (see Refs. 15 and 32 for a comprehensive list of studies). Note that the earlier studies report different values (see Sec. A 3 in Appendix A for more details) of β because in their experiments, the aspect ratio is unity and unlike the current study the value of aspect ratio does not change with the change of the Rayleigh number.

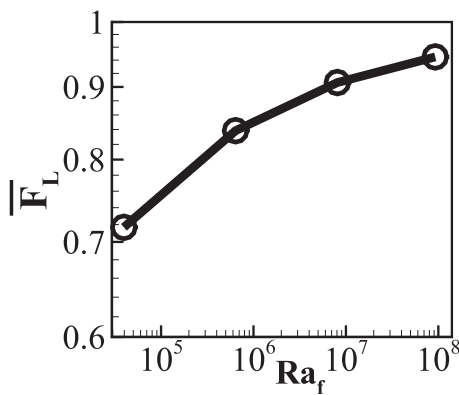


FIG. 21. Plot of time-averaged global liquid volume fraction at the stationary state vs Ra_f for the phase-change RB system at $\text{Ste} = 1.14 \times 10^{-1}$.

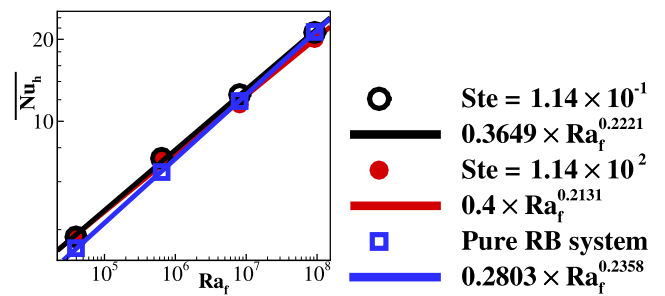


FIG. 22. Plot of the time-averaged Nusselt number for pure RB convection ($\overline{\text{Nu}}_h^{\text{RB}}$) and for RB with phase-change $\overline{\text{Nu}}_h$ at the steady-state vs Ra_f . The best fit curve (continuous blue line) shows that for the classical RB convection is $\overline{\text{Nu}}_h^{\text{RB}} = 0.2803 \times \text{Ra}_f^{0.2358}$ and for the phase-change RB system is $\overline{\text{Nu}}_h = 0.3649 \times \text{Ra}_f^{0.2221}$ (at $\text{Ste} = 1.14 \times 10^{-1}$), and $\overline{\text{Nu}}_h = 0.3649 \times \text{Ra}_f^{0.2131}$ (at $\text{Ste} = 1.14 \times 10^2$) for $3.96 \times 10^4 \leq \text{Ra}_f \leq 9.26 \times 10^7$, and at $\text{Pr} = 0.0216$.

IV. CONCLUSIONS

We have performed two-dimensional direct numerical simulations to systematically compare the phase-change Rayleigh–Bénard convection with the classical Rayleigh–Bénard convection. The total temperature difference in the phase change Rayleigh–Bénard convection system is equally divided between the liquid layer and the solid crust on top separated by an oscillating solid-liquid interface. The presence of the oscillating solid-liquid interface makes the Rayleigh–Bénard convection system different from the classical Rayleigh–Bénard convection of the same average liquid volume, same average aspect ratio, and having same temperature difference across the liquid. The current work attempts to study the influence of the oscillating solid-liquid interface on the Rayleigh–Bénard convection. The Rayleigh number Ra_f defined based on melt height and the Stefan number Ste are the control parameters which are systematically varied in the range $3.96 \times 10^4 \leq Ra_f \leq 9.26 \times 10^7$ and $1.1 \times 10^{-2} \leq Ste \leq 1.1 \times 10^2$ to understand its influence on the heat transport and flow features at $Pr = 0.02$ in the phase-change RB convection.

The phase-change Rayleigh–Bénard convection with an oscillating solid-liquid interface serving as the cold top isothermal boundary demonstrates transient multicellular convective flow patterns encompassing the range from the oscillatory laminar flow regime at low Ra_f to the turbulent flow regime at high Ra_f . The spatio-temporal oscillations of the solid-liquid interface are governed by both the Stefan number Ste and Rayleigh number Ra_f . These spatio-temporal oscillations are seen to modify the classical RB convection by several nontrivial ways and demonstrate a rich interplay between fluid dynamics and thermal transport. The frequency power spectrum of the oscillating solid-liquid interface shows that the intensity of the solid-liquid interface oscillation increases with the increase in the Stefan number and both the frequency and intensity of the solid-liquid interface oscillation increases with Ra_f .

The study reveals that there are several time scales of transport—one associated with the buoyancy-driven bulk flow and its fluctuations depend on Ra_f and another the fluctuation of the solid-liquid interface influenced by the Stefan number. It was shown that the phase-change RB system differs from the classical RB system in two aspects: (1) the top-cold boundary is curved (for the equivalent pure RB system, top-cold boundary is flat), and (2) the solid-liquid interface oscillates as a consequence of latent heat absorption (or release) at multiple frequencies which influences the velocity and temperature field. However, the combination of Ste and Ra_f influences extensively the aspects mentioned above, and they finally decide the heat transport performance of the phase-change RB system with respect to the classical RB system.

Following are important inferences that could be drawn from the current study:

1. It was found that Rayleigh–Bénard convection with a curved top-boundary has a better heat transfer performance as compared to the flat top boundary Rayleigh–Bénard convection. The value of the ratio of the time-averaged Nusselt number at the hot wall for the phase-change RB system, \overline{Nu}_h , to the time-averaged Nusselt number at the hot wall for the classical RB system $\overline{Nu}_h/\overline{Nu}_h^{RB}$ reduces with the increase in Ra_f

as the solid-liquid interface become relatively flatter with the increase in the Rayleigh number Ra_f . For a given average interface height, a larger curvature of the solid-liquid interface not only facilitates more cold contact area to relatively hot fluid but can also accommodate a bigger cell which has relatively higher buoyancy forces as its cell-based Rayleigh number is higher than the cell-based Rayleigh number for the equivalent classical RB system. The phase-change RB system always shows a curved solid-liquid interface in the time-averaged temperature field. However, the ratio $\overline{Nu}_h/\overline{Nu}_h^{RB}$, i.e., the ratio of the time-averaged Nusselt number at the hot wall for the phase-change RB system, \overline{Nu}_h , to the time-averaged Nusselt number at the hot wall for the classical RB system, \overline{Nu}_h^{RB} , at the stationary state is greater than unity only if the form of the curvature is stable throughout the stationary state. Depending on the laminar or turbulent flow regime, there are two kinds of solid-liquid interface and Rayleigh–Bénard convection interactions as described below.

- (a) For the phase-change RB system with laminar Rayleigh–Bénard convection, irrespective of the Stefan number, it is observed that the form of the curvature is stable throughout the stationary state and thus the ratio of $\overline{Nu}_h/\overline{Nu}_h^{RB}$ is always greater than one.
- (b) For the phase-change RB system with turbulent Rayleigh–Bénard convection, the $\overline{Nu}_h/\overline{Nu}_h^{RB}$ ratio can be greater (or lower) than unity for $Ste < 1.14$ (or $Ste > 1.14$). It is observed that for a very low Stefan number ($Ste < 1.14$), the form of the curvature is stable throughout the stationary state and thus $\overline{Nu}_h/\overline{Nu}_h^{RB}$ is greater than one. However, for the phase-change RB system with turbulent Rayleigh–Bénard convection for a high-value Ste ($Ste > 1.14$), drastic and dynamic changes in the form of the curvature are observed, multiple inflection points on the solid-liquid interface are seen where locally the concave surface changes to the convex surface during the stationary state. It is seen that such drastic dynamic changes in the form of the curvature are detrimental to the large-scale convection currents and the heat transfer performance in the phase-change Rayleigh–Bénard convection.
2. The stationary state time-averaged global liquid volume fraction $\overline{F_L}$ for the phase-change RB system increases with the increase of Ra_f ; and at higher Ra_f , $\overline{F_L}$ tends to approach a value of unity.
3. The Nusselt number for both the phase-change RB system and pure RB system is seen to increase with Ra_f , and the best fit shows a power-law scaling $\overline{Nu}_h^{RB} \propto Ra_f^{0.2358}$ for the classical RB system, $\overline{Nu}_h \propto Ra_f^{0.2221}$ (at $Ste = 1.14 \times 10^{-1}$) and $\overline{Nu}_h \propto Ra_f^{0.2131}$ (at $Ste = 1.14 \times 10^2$) for the phase-change RB system. The exponent of Ra_f for the classical RB system is 9.62% and 6.17% higher as compared to the high Stefan number case (at $Ste = 1.14 \times 10^2$) and at the low Stefan number case (at $Ste = 1.14 \times 10^{-1}$) of the phase-change RB system, respectively. For $Ra_f \geq 8.08 \times 10^6$, in the turbulent Rayleigh–Bénard convection regime, the difference in the value of \overline{Nu}_h for the high Stefan number case (at $Ste = 1.14 \times 10^2$) and at the low Stefan

- number case (at $\text{Ste} = 1.14 \times 10^{-1}$) reduces with the increase in Ra_f . Also, with the increase in Ra_f , the values of \overline{Nu}_h for the phase-change system are very close to the pure RB system (see Table I); this is because at higher Rayleigh number ($Ra_f = 9.26 \times 10^7$), the solid-liquid interface is very close to top boundary ($F_L = 0.95$), subjected to high-temperature gradients which restrict the fluctuations of the solid-liquid interface.
4. At $Ra_f = 3.96 \times 10^4$, the flow is unsteady laminar with the fluid domain average aspect ratio of 0.72. There are two distinct RB flow configurations at low Ra_f independent of Ste—flow configuration-P and flow configuration-Q (see Fig. 5). For flow configuration-P, the hot liquid rises near the central region, touches the top interface boundary, and the cooler liquid sinks down along a vertical wall and forms the main convection cell. For flow configuration-Q, the hot liquid rises along a vertical wall and the cooler liquid sinks near the central region forming the main convection cell. Compared to the classical RB system, \overline{Nu}_h for the phase-change RB system increases by 10% for flow configuration-P and 15% for flow configuration-Q.
 5. At $Ra_f = 8.08 \times 10^6$, the flow is turbulent with the fluid domain average aspect ratio of 0.91. As compared to lower Ra_f , the solid-liquid interface is slightly curved but fluctuates for phase change Rayleigh–Bénard convection. As compared to the classical Rayleigh–Bénard convection, \overline{Nu}_h for phase change Rayleigh–Bénard convection increases by upto 7% for $\text{Ste} < 1$ and decreases by upto 2% for $\text{Ste} \geq 1$. For $\text{Ste} < 1$ (or for $\text{Ste} \geq 1$), the form of the curvature of the solid-liquid interface is retained (is not retained) throughout the stationary state as the strength of solid-liquid interface oscillations is low (high). At high Stefan numbers ($\text{Ste} \geq 1$), multiple inflection points are observed on the solid-liquid interface, which are detrimental to the large-scale convective currents.

For the studied range of Ra and Ste with the low Prandtl number, the current study shows that when the flow field is not turbulent, the phase-change Rayleigh–Bénard system has higher heat transport as compared to the classical RB system. This understanding is crucial not only for the man-made applications such as electronic and nuclear-reactor cooling systems, phase-change-based passive cooling systems in buildings, modern PCM-based-clothing, and energy storage systems but also this knowledge may have far-ranging implications in the understanding of natural geophysical and astrophysical systems like phase-change processes in earth's mantle, partial or complete freezing/melting of water bodies, melting of polar ice caps, etc.^{4,5,19,43} Also, the current results suggest that the thermal systems with RB convection will have better heat transfer performance with curved-top-boundary instead of flat-top-boundary. Later, the current work can be extended for a moderate and high Prandtl number phase-change Rayleigh–Bénard convection system which may yield very different results as compared to the present study.

SUPPLEMENTARY MATERIAL

The supplementary material comprises of three Appendices: (A) Verification and validation of code, (B) grid details for RB convection inside the curved container, and (C) Frequency power spectrum of global melt fractions. Each Appendix is described in the

main manuscript, in the respective section of the manuscript where the Appendix is cross-referred/cited.

REFERENCES

- ¹K.-I. Ahn, D.-H. Kim, B. Kim, and C. Sohn, "Numerical investigation on the heat transfer characteristics of a liquid-metal pool subjected to a partial solidification process," *Prog. Nucl. Energy* **44**, 277 (2004).
- ²J. Batina, S. Blancher, and T. Kouskou, "Modelling of a phase change material melting process heated from below using spectral collocation methods," *Int. J. Numer. Methods Heat Fluid Flow* **24**, 697 (2014).
- ³A. Brent, V. Voller, and K. Reid, "Enthalpy-porosity technique for modeling convection-diffusion phase change: Application to the melting of a pure metal," *Numer. Heat Transfer, Part A* **13**, 297 (1988).
- ⁴S. H. Davis, *Theory of Solidification* (Cambridge University Press, 2001).
- ⁵S. H. Davis, H. Huppert, U. Müller, and M. Worster, *Interactive Dynamics of Convection and Solidification* (Springer Science & Business Media, 2012), Vol. 219.
- ⁶C. Dietsche and U. Müller, "Influence of Bénard convection on solid–liquid interfaces," *J. Fluid Mech.* **161**, 249 (1985).
- ⁷R. Farhadieh and R. Tankin, "A study of the freezing of sea water," *J. Fluid Mech.* **71**, 293 (1975).
- ⁸B. Favier, J. Purseed, and L. Duchemin, "Rayleigh–Bénard convection with a melting boundary," *J. Fluid Mech.* **858**, 437 (2019).
- ⁹J. H. Ferziger and M. Peric, *Computational Methods for Fluid Dynamics*, 3rd ed. (Springer, 2001).
- ¹⁰S. Grossmann and D. Lohse, "On geometry effects in Rayleigh–Bénard convection," *J. Fluid Mech.* **486**, 105 (2003).
- ¹¹E. Holzbecher, "Convection pattern formation in a domain with a horizontal interface," *Phys. Fluids* **31**, 056602 (2019).
- ¹²H. E. Huppert, "The fluid mechanics of solidification," *J. Fluid Mech.* **212**, 209 (1990).
- ¹³H. Jasak, "Error analysis and estimation for the finite volume method with applications to fluid flows," Ph.D. thesis, Department of Mechanical Engineering Imperial College of Science, Technology and Medicine, 1996.
- ¹⁴R. M. Kerr and J. R. Herring, "Prandtl number dependence of Nusselt number in direct numerical simulations," *J. Fluid Mech.* **419**, 325 (2000).
- ¹⁵E. M. King and J. M. Aurnou, "Turbulent convection in liquid metal with and without rotation," *Proc. Natl. Acad. Sci. U. S. A.* **110**, 6688 (2013).
- ¹⁶V. Kumar, M. Kumawat, A. Srivastava, and S. Karagadde, "Mechanism of flow reversal during solidification of an anomalous liquid," *Phys. Fluids* **29**, 123603 (2017).
- ¹⁷V. Kumar, A. Srivastava, and S. Karagadde, "Compositional dependency of double-diffusive layers during binary alloy solidification: Full field measurements and quantification," *Phys. Fluids* **30**, 113603 (2018).
- ¹⁸S. Labrosse, J. Hernlund, and N. Coltice, "A crystallizing dense magma ocean at the base of the earths mantle," *Nature* **450**, 866 (2007).
- ¹⁹A. Mazzino, "Two-dimensional turbulent convection," *Phys. Fluids* **29**, 111102 (2017).
- ²⁰C. D. McConnochie and R. C. Kerr, "The effect of a salinity gradient on the dissolution of a vertical ice face," *J. Fluid Mech.* **791**, 589 (2016).
- ²¹W. Minkowycz, *Advances in Numerical Heat Transfer* (CRC Press, 1996), Vol. 1.
- ²²F. Moukalled, L. Mangani, M. Darwish *et al.*, *The Finite Volume Method in Computational Fluid Dynamics* (Springer, 2016).
- ²³E. P. van der Poel, R. J. Stevens, and D. Lohse, "Comparison between two- and three-dimensional Rayleigh–Bénard convection," *J. Fluid Mech.* **736**, 177 (2013).
- ²⁴E. P. van der Poel, R. J. Stevens, K. Sugiyama, and D. Lohse, "Flow states in two-dimensional Rayleigh–Bénard convection as a function of aspect-ratio and Rayleigh number," *Phys. Fluids* **24**, 085104 (2012).
- ²⁵C. Prakash, M. Samonds, and A. Singhal, "A fixed grid numerical methodology for phase change problems involving a moving heat source," *Int. J. Heat Mass Transfer* **30**, 2690 (1987).

- ²⁶O. Satbhai, "Heat transfer model for laser surface remelting: Towards a multi-scale solidification model," M.Sc. thesis, Indian Institute of Technology, Kharagpur, 2013.
- ²⁷O. Satbhai, S. Roy, and S. Ghosh, "Numerical simulation of laser surface remelting on unstructured grids," *Trans. Indian Inst. Met.* **65**, 833 (2012).
- ²⁸O. Satbhai, S. Roy, and S. Ghosh, in *ASME 2017 International Mechanical Engineering Congress and Exposition* (American Society of Mechanical Engineers, 2017), pp. V008T10A055.
- ²⁹O. Satbhai, S. Roy, and S. Ghosh, "A parametric multi-scale, multiphysics numerical investigation in a casting process for Al-Si alloy and a macroscopic approach for prediction of ECT and CET events," *Appl. Therm. Eng.* **113**, 386 (2017).
- ³⁰O. Satbhai, S. Roy, and S. Ghosh, "Role of heating location on the performance of a natural convection driven melting process inside a square shaped thermal energy storage system," *J. Therm. Sci. Eng. Appl.* **10**, 061007 (2018).
- ³¹O. Satbhai, S. Roy, and S. Ghosh, "Direct numerical simulation of a low Prandtl number Rayleigh–Bénard convection in a square box," *J. Therm. Sci. Eng. Appl.* **11**, 061004 (2019).
- ³²J. D. Scheel and J. Schumacher, "Global and local statistics in turbulent convection at low Prandtl numbers," *J. Fluid Mech.* **802**, 147 (2016).
- ³³J. Schmalzl, M. Breuer, and U. Hansen, "On the validity of two-dimensional numerical approaches to time-dependent thermal convection," *Europhys. Lett.* **67**, 390 (2004).
- ³⁴C. Swaminathan and V. Voller, "On the enthalpy method," *Int. J. Numer. Methods Heat Fluid Flow* **3**, 233 (1993).
- ³⁵F. Tan and C. Tso, "Cooling of mobile electronic devices using phase change materials," *Appl. Therm. Eng.* **24**, 159 (2004).
- ³⁶M. Torabi Rad, "Solidification melting source: A built-in fv option in openfoam® for simulating isothermal solidification," in *OpenFOAM®: Selected Papers of the 11th Workshop*, edited by J. M. Nóbrega and H. Jasak (Springer International Publishing, Cham, 2019), pp. 455–464.
- ³⁷M. Ulvrová, S. Labrosse, N. Coltice, P. Rábæk, and P. Tackley, "Numerical modelling of convection interacting with a melting and solidification front: Application to the thermal evolution of the basal magma ocean," *Phys. Earth Planet. Inter.* **206**, 51 (2012).
- ³⁸G. Vasil and M. Proctor, "Dynamic bifurcations and pattern formation in melting-boundary convection," *J. Fluid Mech.* **686**, 77 (2011).
- ³⁹V. Voller, A. Brent, and C. Prakash, "The modelling of heat, mass and solute transport in solidification systems," *Int. J. Heat Mass Transfer* **32**, 1719 (1989).
- ⁴⁰V. Voller and C. Prakash, "A fixed grid numerical modelling methodology for convection-diffusion mushy region phase-change problems," *Int. J. Heat Mass Transfer* **30**, 1709 (1987).
- ⁴¹F. Waleffe, A. Boonkasame, and L. M. Smith, "Heat transport by coherent Rayleigh–Bénard convection," *Phys. Fluids* **27**, 051702 (2015).
- ⁴²M. G. Worster, "Convection in mushy layers," *Annu. Rev. Fluid Mech.* **29**, 91 (1997).
- ⁴³L. Yao and J. Prusa, "Melting and freezing," *Adv. Heat Transfer* **19**, 1 (1989).
- ⁴⁴B. Zalba, J. M. Marín, L. F. Cabeza, and H. Mehling, "Review on thermal energy storage with phase change: Materials, heat transfer analysis and applications," *Appl. Therm. Eng.* **23**, 251 (2003).
- ⁴⁵Q. Zhou, B.-F. Liu, C.-M. Li, and B.-C. Zhong, "Aspect ratio dependence of heat transport by turbulent Rayleigh–Bénard convection in rectangular cells," *J. Fluid Mech.* **710**, 260 (2012).